Carbon Nanotube Alignment: Electromagnetic Field and Shear Force

by

Yipeng He

A dissertation submitted in partial fulfillment
of the requirements for the degree of
Doctor of Philosophy
(Materials Science and Engineering)
in the University of Michigan
2019

Doctoral Committee:

Professor Alan I. Taub, Chair
Professor John Halloran
Professor John Kieffer
Professor Wei Lu

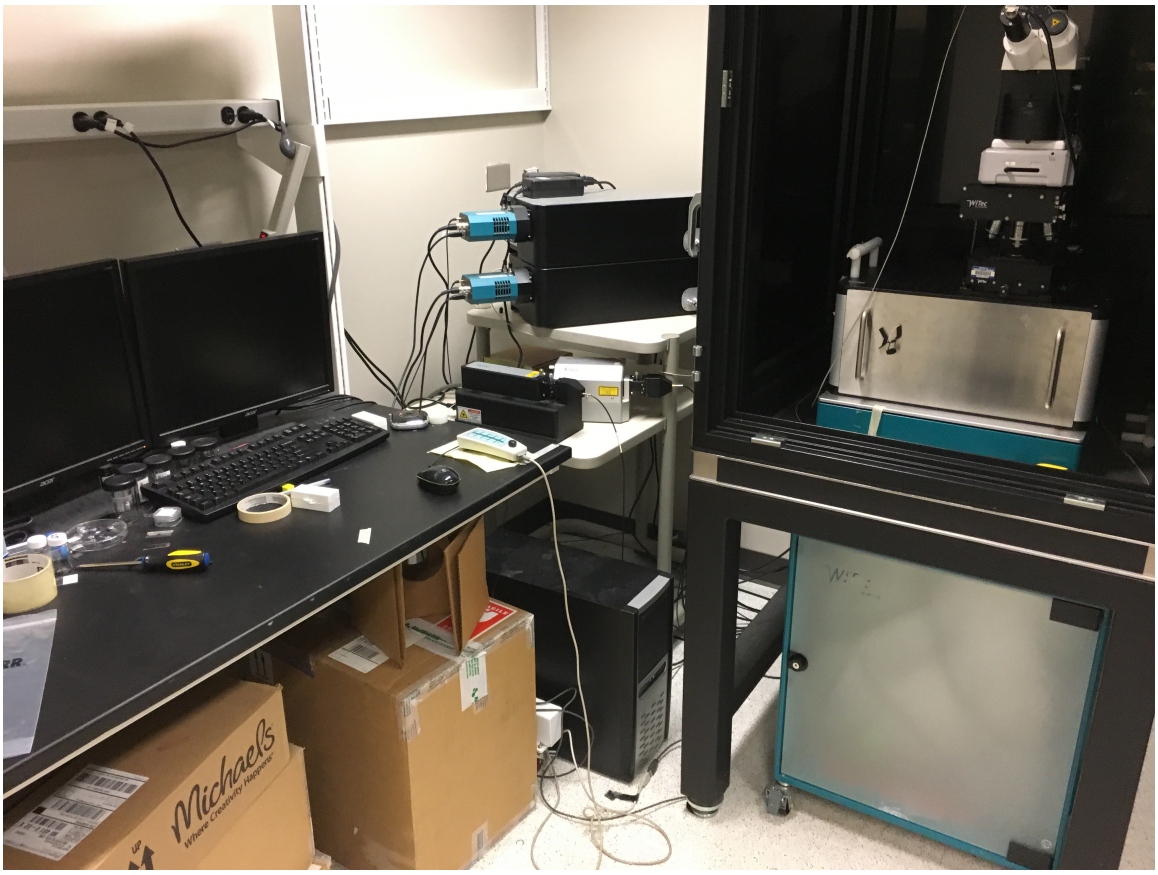

Where I spent years.

Yipeng He

oliverhe@umich.edu

ORCID: 0000-0001-6725-6105

To everyone I met, who saved and helped me, my unknown brother in Japan, my friends and family, and myself.

Life is good, powered by optimism.

ACKNOWLEDGEMENTS

First, I would like to express my deepest gratitude to my advisor, Prof. Alan Taub, without whom, none of these would have happened. I am grateful for your time, patience and guidance. The research freedom and inspiring ideas you have given are something I would never forget. I would miss the quick-and-dirty experiments we had for fun. I would also like to thank the rest of my thesis committee: Prof. John Halloran, Prof. John Kieffer and Prof. Wei Lu. And Prof. Levi Thompson served on my prelim committee (now at the University of Delaware). I have the privilege to learn a lot from you through helpful discussions.

It took a huge amount of effort to make our real-time Raman spectroscopy work and we received tremendous help around the campus. I am grateful for: Prof. John Kieffer, Dr. Weimin Wang and Dr. Michael Aldridge, for setting up early-stage Raman experiments; Prof. Wei Lu for providing the electrical equipment during the early stage; Prof. Joerg Lahann and Dr. Nathan Jones for help and access to the Raman room; Prof. Ronald Larson for insightful discussions that lead to us using the Linkam shearing stage that saved my research; Prof. Michael Solomon and Dr. Yufei Wei for help and access to the viscometer; Dr. Wei Liu and Tavis Ezell for WITec tech support; and John Hart for the tech support of the Linkam shearing stage.

I would like to sincerely thank my colleagues and friends in our fabulous Taub group. Current members: Dr. Maya Nath, Avi Bregman, Randy Chen, Aaron Gladstein, Amy Langhorst, Anita Luong, Caleb Reese, Anshul Singhal, and Dandan Zhang. Alumni: Dr. Daniel McNerny, Dr. Xun Liu, Dr. Wesley Chapkin, Erika

Salem, and Tasha Mangaldas.

I also want to acknowledge the staff members at the University of Michigan who have offered numerous help so I can concentrate on my research: Angela Farrehi, Shelley Fellers, Renee Hilgendorf, Debra Johnson, Ellen Kampf and Keith McIntyre.

I took a detour in 2017 and cannot thank enough everyone I met at the University Hospital: doctors, nurses, social workers and all other staff members. Special thanks to Dr. Patrick Burke, Dr. Sarah Anand and Dr. Jennifer Baumhauer.

I would like to thank my awesome friends who supported me through this journey: Yuchi Cui, Fangxiao Dong, Ya Gai, Haocheng Hong, Yuchen Hua, Zhihua Huang, Weichao Kong, Shengyu Lou, Wei Luo, Xin Shen, Guangsha Shi, Yu Sui, Xinyu Tan, Sui Tao, Wenkun Wu, Yang Xu and many many others.

Lastly, I would like to thank my family for their unconditional love and support: my mother, Xiufang Li; my father, Rong He; grandmothers, Yunfen Zhao and Qinxian Weng; grandfathers, Shounan He and Guangen Li; and all of my aunts, uncles and cousins.

TABLE OF CONTENTS

LIST OF FIGURES

Figure

LIST OF TABLES

Table

LIST OF APPENDICES

Appendix

LIST OF ABBREVIATIONS

CNT carbon nanotube

SWCNT single-walled carbon nanotube

MWCNT multi-walled carbon nanotube

CF carbon fiber

OM optical microscopy

SEM scanning electron microscopy

TEM transmission electron microscopy

RBM radial breathing mode

PSS polystyrene sulfonate

PVA polyvinyl alcohol

DC direct current

AC alternating current

ABSTRACT

Carbon nanotube (CNT)/polymer composites are promising structural materials because of their excellent strength and stiffness. However, the reported data of their strengthening effect is highly scattered. This variability and the high material cost are important inhibitors for wide application of CNT/polymer composites. We aim to improve the cost-property relationship by improving the consistency of strengthening polymer composites by addressing the CNT alignment. CNT alignment has been found to be crucial to the mechanical properties of the composite, e.g. modulus and strength, analogous to the role of carbon fibers in polymer composites.

Previous studies focused on discrete measurements and limited data on alignment kinetics has been reported. We developed an *in situ*, real-time characterization method using Raman spectroscopy to study CNT alignment in a polymer matrix. Alignment methods include electric field, magnetic field and shear force. CNT alignment is characterized in CNT-Polystyrene Sulfonate (PSS)/Polyvinyl Alcohol (PVA) film (discrete measurement) and in CNT/EPON 828 suspension (real-time study), with a focus on the latter. For real-time experiments, the indicator of alignment behavior (changes of G-band intensity) is tracked over time in the alignment direction.

The technique has been successfully applied to study alignment behavior in an AC field. CNT alignment is confirmed through distinct Raman spectra of unaligned (CNTs randomly oriented) and aligned CNT-PSS/PVA films. Real-time alignment behavior is captured in the CNT/EPON 828 mixture. Higher electric field strength leads to faster alignment and a degree of alignment.

Magnetically-induced alignment has been observed in a CNT-PSS/PVA film. For real-time experiments, alignment is not obvious and the Raman signals are more scattered than observations from electric field experiments. This is due to both the low magnetic susceptibility of our pristine CNTs and the translational motion of CNTs. Further studies are needed using higher field magnets or high susceptibility CNTs. For example, CNTs coated or infiltrated with magnetic nanoparticles.

CNT alignment has also been successfully characterized in a shear flow. Alignment behaviors are similar to the observations in electric field. Higher shear rate results in faster alignment and a greater degree of alignment. Higher temperature lowers the degree of alignment but does not affect the alignment speed. These two effects agree with the Péclet number and our model of driving force for alignment. Moreover, the alignment is reversible and reproducible in response to changes of shear rate and temperature. Unusual alignment behaviors were found under high shears and at low or high temperatures. Further investigation is needed to determine the CNT behavior in these situations. A comparison between shear force alignment and its electric field counterpart shows similar alignment kinetics but different driving forces. In both cases, thermal randomization occurs immediately when the applied field is discontinued, suggesting the need to maintain the field in order to capture the full potential of alignment for composite manufacturing.

CHAPTER I

Introduction

1.1 Introduction

1.1.1 CNT and CNT/Polymer Composite

Extensive research effort has been devoted to carbon nanotubes (CNTs) since their discovery by Iijima in 1991 [1]. CNTs have a unique quasi one-dimensional nanoscale structure and are highly anisotropic. Their remarkable mechanical [2, 3], electrical [4] and thermal [5] properties may enable a large variety of applications, including random access memory (RAM), atomic force microscopy (AFM) tips, battery electrodes, super capacitors, solar cells, and reinforcements for composite materials.

Numerous investigations have been done on various CNT/polymer composites and significant property enhancement is observed due to the addition of CNTs [2, 6–8]. CNTs have also seen limited use in commercial applications including bicycle frames, airframe components and hulls for maritime security boats [9].

Despite its amazing ability of property enhancement, the application of CNTs have not seen widespread adoption due to (1) composite properties falling below the strengthening expected based on individual CNT measurements, (2) manufacturing hurdles at high volume, and (3) the high price of the CNTs [10].

1.1.2 Strengthening Variability

In order to improve the property/cost ratio, attention must be focused on developing scalable CNT production and processing methods as well as further optimizing the mechanical properties of CNT composites. Efforts have been made to investigate various CNT/polymer systems and alignment methods, but the data reported are highly variable [11]. For example, Figure 1.1 (data from [11]) illustrates CNTs strengthening effect for strength and modulus. Each color represents a literature value referenced in [11], marked by the CNT weight fraction. The same CNT loading, e.g. 0.2%, can result in different strength and modulus improvement and higher loading does not necessarily lead to better strengthing.

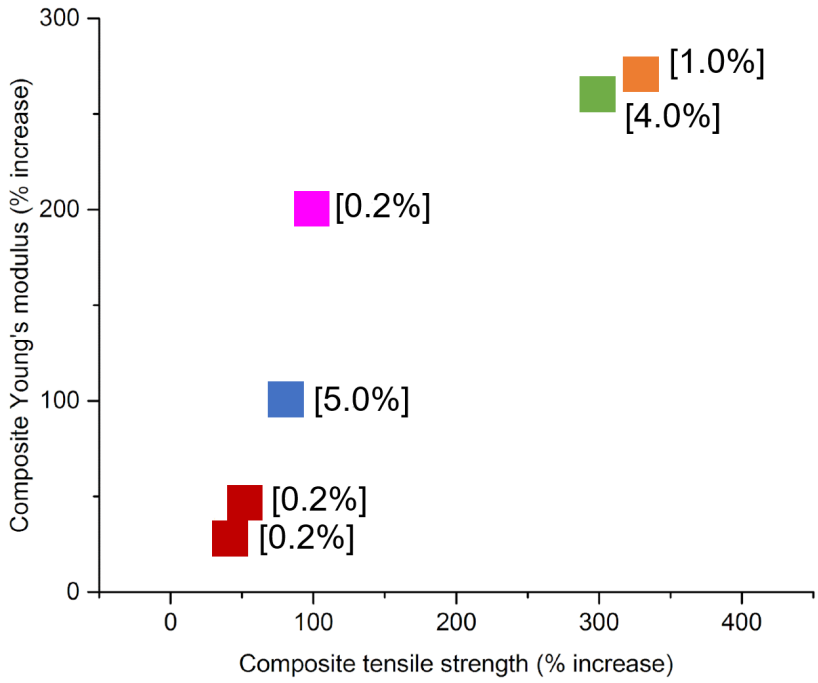

Figure 1.1: Strengthening effect of CNT for strength and modulus. Each color represents a literature, marked by the CNT weight fraction, from [11].

The variability can be attributed to a number of factors, including differing physical properties of the CNTs and polymer matrices that can be very different from different suppliers as well as variability in dispersion.

CNTs potential as a reinforcement have not been fully achieved (e.g. dispersion and alignment issues) and standard protocols and optimal fabrication methods (e.g. CNT loading and CNT-matrix interface) have to be developed.

1.1.3 Materials Cost

The prices of single-walled carbon nanotube (SWCNT) and multi-walled carbon nanotube (MWCNT) are in the range of \$50-400/g and \$0.1-25/g (2013 from [10]), about 1- to 10-fold greater than commercially available carbon fiber (CF).

Despite currently high costs of CNTs [9], CNT composites are expected to become cost-effective with improved manufacturing techniques and optimized fabrication process. Moreover, CNT costs will be gradually lowered through increased production capacity (Figure 1.2).

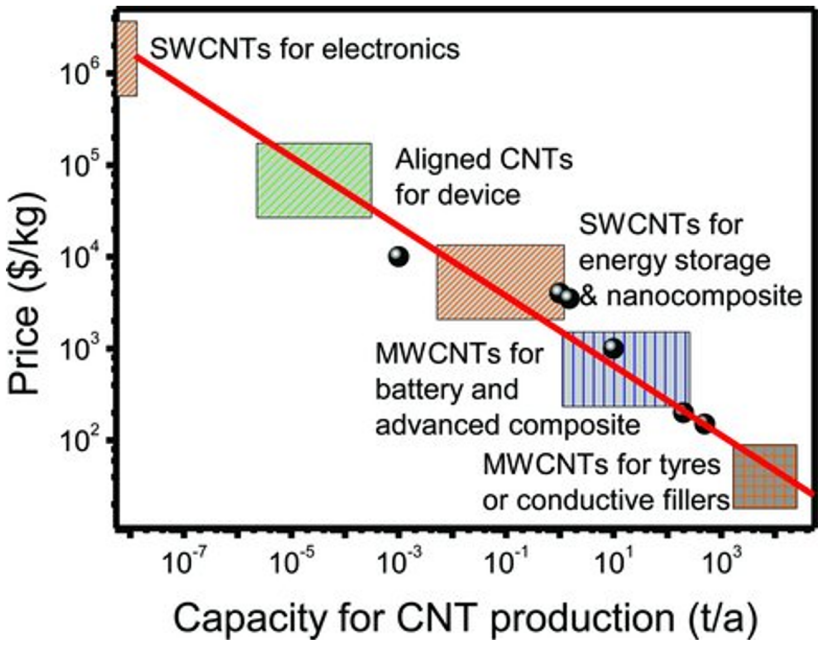

Figure 1.2: Linear relationship between productivity and prices of CNTs from a double-logarithmic-coordinate plot [10].

1.1.4 Motivation

The motivation of our research is to address the issues of strengthening variability and high materials cost (see Appendix A) by fulfilling CNTs potential as a structural reinforcement and consistently making mechanically-strong polymer composites. This work focuses on one of the most important factors in determining the composite property: CNT alignment. The goal is to understand the kinetics of CNT alignment in a polymer matrix through real-time characterization of alignment. This knowledge is expected to provide helpful guidance for fabricating aligned CNT composites, in which CNTs provide a consistent strengthening effect, similar to the role of CF in CF-reinforced composites.

1.2 Background

The unique structure of CNT's gives highly anisotropic properties. The strength and stiffness along the tube axis is much higher than those along transverse direction [12]. The alignment of CNTs in a polymer matrix increases the tensile strength and Youngs modulus of the composite in the direction of the alignment [13–16]. The alignment of CNTs is associated with the orientation of the tube (or bundle) axis, similar to fiber orientation in composites. It is hypothesized that optimal performance will involve CNTs that are randomly distributed in the polymer matrix but are aligned in a direction induced by external forces on that direction. The CNT loadings are kept at low level, usually less than 5 wt%, because higher loadings have shown an adverse effect on property improvement [14, 15] due to the difficulty of CNT dispersion. It is worth noting other properties, such as electric or thermal properties, are improved from alignment as well. For instance, electrical conductivity in the alignment direction is found to be increased [7, 14].

1.2.1 Alignment Methods

Ajayan first reported a simple method to induce CNT alignment by cutting a CNT/epoxy composite with a diamond knife and a microtome [17]. The directional cutting process created shear that induces flow of material. The CNTs were deformed by shear and were oriented unidirectionally. Since then, various methods have been reported to induce CNT alignment in polymer matrix, including electric field [7, 14, 18–21], magnetic field [22–27], mechanical methods (shear) [13, 15, 17, 28–35] and aligned growth [36]. Combinations of these methods have also been explored [37, 38].

These aligning techniques can be classified into two groups [12, 39]: 1) *in situ* alignment where CNTs are aligned during growth and then compounded with polymer matrix (aligned growth) and 2) *ex situ* alignment where CNTs are first randomly distributed in polymer and alignment is induced afterwards, e.g. during the curing process using applied forces. *In situ* alignment techniques are simple to employ but suffer from growth restrictions such as substrate material and temperature and sample transfer. *Ex situ* alignment techniques involve the acquisition of commercially available CNTs. They are free of growth restriction and importantly, easier to scale up. This work focuses on *ex situ* alignment, including electric field (Chapter III), magnetic field (Chapter IV) and shear force (Chapter V).

1.2.2 Alignment Characterization

CNT alignment characterization methods can be classified into *direct* and *indirect* methods.

1.2.2.1 Direct Methods

Direct methods provide an examination of CNT alignment and mainly consist of various microscopy methods: optical microscopy (OM), scanning electron microscopy (SEM), transmission electron microscopy (TEM), etc. Figure 1.3 shows CNT alignment

under OM (Figure 1.3(a)[20]), SEM (Figure 1.3 (b)[25]), and TEM (aligned bundle, Figure 1.3 (c)[40]). OM has a relatively low resolution limit and only CNT bundles or aggregates are seen. SEM and TEM, however, have higher resolutions and are able to identify individual CNTs. They are typically used to characterize solid specimens and it is difficult to set up real-time observations. There are *in situ* TEM techniques [41, 42] that might prove useful to observe CNT alignment in polymer matrix but we are not aware of any studies of this kind. Microscopic methods offer qualitative measurement of CNT alignment. To generate a convincing quantitative estimation of the degree of alignment, one might need to analyze a large number of microscopy images, which is tedious and time-consuming.

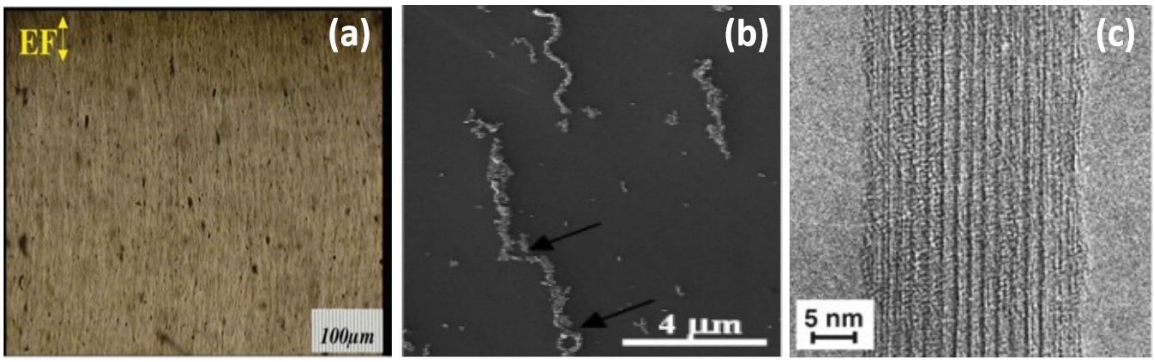

Figure 1.3: CNT alignment under different microscopies: (a) OM [20], (b) SEM [25] and (c) TEM (aligned bundle, [40]). External force is applied in the vertical direction for (a) and (b).

1.2.2.2 Indirect Methods

Indirect methods for CNT alignment characterization include X-ray diffraction and polarized Raman spectroscopy.

X-ray X-ray diffraction is a quantitative technique that can determine the orientation and the degree of CNT alignment [29]. The diffraction intensity is almost a constant for all Azimuth angles if CNTs are randomly aligned (Figure 1.4(a)). When CNTs

are aligned, the intensity presents two peaks at the angles of 90^o and 270^o (X-ray source perpendicular to CNT alignment) (Figure 1.4(b)). The total number of aligned CNTs is proportional to the integrated intensity of the two peaks in Figure 1.4(b). The X-ray interacts primarily with the electron shells of the carbon atoms. Due to the small number of electrons outside a carbon atom, the intensity of the scattered X-ray is low. Therefore, X-ray diffraction is used to characterize CNT forests or composites containing high a weight fraction of CNTs. In addition, X-ray diffraction is performed on solid samples. We have not seen any examples of X-ray diffraction for CNT solution studies.

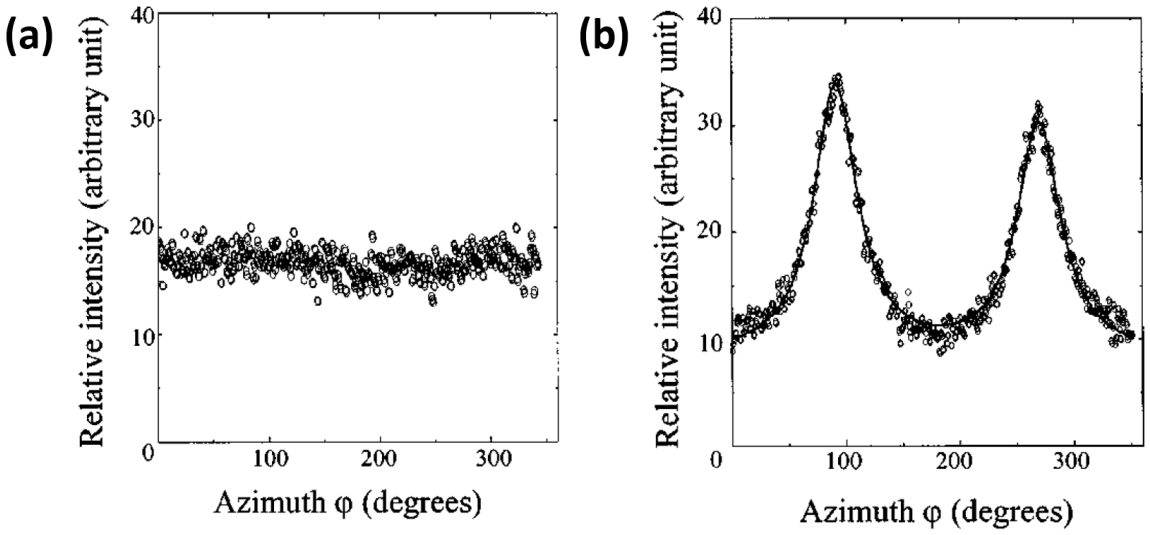

Figure 1.4: X-ray diffraction patterns of (a) randomly aligned CNTs and (b) aligned CNTs in PHAE matrices. The CNTs are aligned by a stretching method [29].

Polarized Raman Spectroscopy Raman spectroscopy is an inelastic spectroscopy technique, in which the laser light is usually polarized to identify anisotropic material properties (additional details are provided in Chapter II). Previous Raman spectroscopy studies have been on solid samples but the technique is amenable to include real-time observation on liquid samples. Advantages of performing real-time study on Raman

spectroscopy over other characterization techniques are:

- Raman spectroscopy has good spatial resolution ($\sim$0.5 μm) and sensitivity (individual CNTs).
- It offers quantitative measurement of the CNT alignment with a fast data acquisition, ideal for kinetics studies.
- Energy of the excitation source is relatively low as compared to the electron beams in SEM/TEM or the X-rays in X-ray diffraction. This lowers the chance of sample damage and raising the temperature in the liquid samples.
- Experiments can be conducted in ambient environment (vacuum not needed), making it easier to set up *in situ* measurements.

1.3 Research Overview

The overall goal of this research is to improve cost-property enhancement and consistency of CNT composite materials. This work focuses on CNT alignment, which has the potential to improve mechanical properties and consistency of CNT composites. Challenges for the kinetics study of alignment when we started the project include:

- Lack of an effective real-time characterization method: The majority of previous research in the field has only characterized cured solid products. Traditional material characterization techniques, e.g. OM, SEM, TEM, X-ray and etc., are not suitable for real-time experiments.
- Lack of a systematic study of alignment methods: various alignment methods have been proposed, but not fully assessed and compared.

To overcome the above challenges, we aimed to:

- Develop an *in situ* method to observe real-time orientation of CNTs and quantitatively characterize the degree of alignment.
- Use the *in situ* characterization method to study the CNT alignment and develop a phenomenological model.
- Compare CNT alignment under electric field, magnetic field and shear force.

1.4 Thesis Overview

The real-time Raman spectroscopy we developed, as well as its application to study alignment behavior under various external forces, is described in this thesis. Chapter II gives a comprehensive literature review of Raman Spectroscopy and its application on CNT composites. Then an overview of our real-time Raman characterization technique is presented. Chapter III presents our first study on electric field alignment. CNT alignment is first observed in solid samples and then successfully captured in real time, demonstrating the effectiveness of our technique. In Chapter IV, our attempts to study magnetic field alignment are described. The degree of alignment was found to be scattered and smaller than that from the electric field. Discussions and directions for future study of magnetic field alignment are given. Chapter V presents the study of shear-induced alignment. The alignment kinetics is investigated in detail, and compared to its electric field counterpart. Finally, Chapter VI summarizes this thesis and gives an outlook for future research on CNT alignment.

CHAPTER II

Polarized Raman Spectroscopy

2.1 Introduction

Raman spectroscopy is a spectroscopic technique that observes vibrational modes of material systems [43]. When photons are scattered from the atom or molecule, the majority of them are elastically scattered, which is referred to as Rayleigh scattering. The frequency or wavelength of the photons are not changed during the scattering. A small portion of the photons, however, are inelastically scattered, the Raman scattering. The frequency or wavelength of the inelastically scattered photons are different from the incoming photons. There are two types of Raman scattering. The photons resulting from inelastic scattering can be either of higher (anti-Stokes Raman) or lower (Stokes Raman) energy of the incident photons. Figure 2.1 is an energy level diagram that compares Infrared absorption, elastic Rayleigh scattering and inelastic Raman scattering (Stokes and Anti-Stokes).

Figure 2.2(a) shows Raman spectra of a metallic and a semiconducting SWCNT [44]. The Raman spectrum of CNT includes the radial breathing mode (RBM), tangential mode (G-band), disorder-induced mode (D-band) and its second overtone (G-band), and other features. The G band comes from the graphitic structure and characterizes in-plane vibration of carbon atoms while RBM characterizes the atomic vibration in the radial direction. As seen from the spectra, the shapes of each

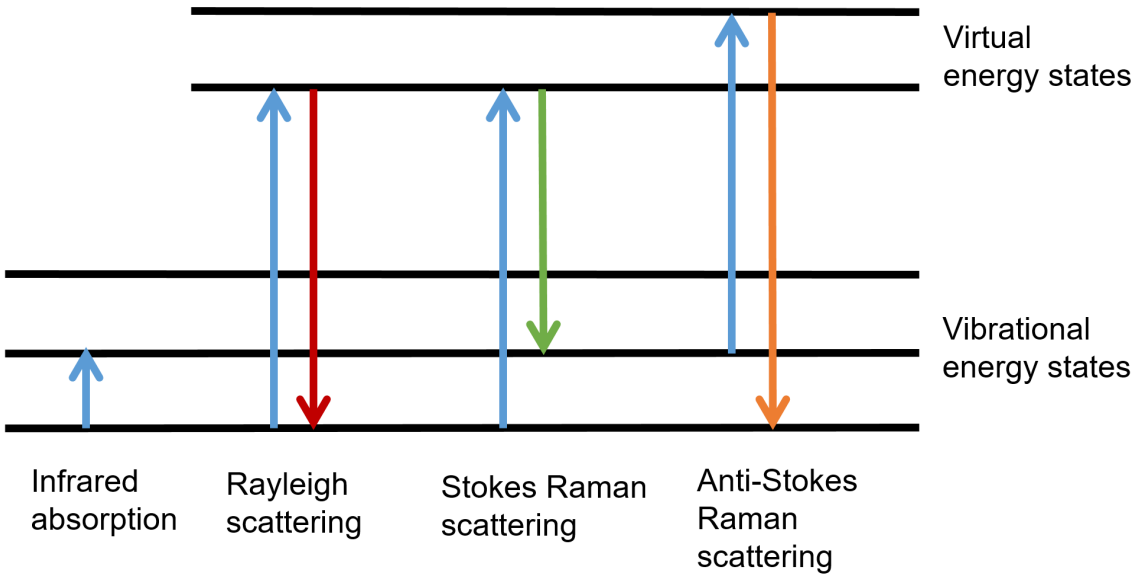

Figure 2.1: Energy level diagram of Infrared absorption, Rayleigh scattering and Stokes and Anti-Stokes Raman scattering.

band and their relative intensities depend on the electronic property of the CNT, i.e. whether its metallic or semiconducting. While graphite is a two-dimensional semimetal, the way of rolling up the graphite sheet (chirality) affects the distribution of density of states (DOS) and results in CNT being metallic or semiconducting along the tubular axis. Figure 2.2(b) is a schematic picture of atomic vibration of RBM mode and the G-band [45]. The name of G-band is misleading: it is given because this mode is usually the second strongest after the G-band in graphite.

SWCNTs consist of two main components in the G-band, called G^+-band ($\sim$ 1590 cm^{-1}) and G^--band ($\sim$ 1570 cm^{-1}) (Figure 2.3) [46]. The G^+-band corresponds to the carbon atom vibrations along the longitudinal axis while the G^--band is associated with vibrations of carbon atoms along the circumferential direction. The lineshape of the G^--band is sensitive to whether the SWCNT is metallic (Breit-Wigner -Fano lineshape, Figure 2.3(a)) or semiconducting (Lorentzian lineshape, Figure 2.3(b)). The G-band for large diameter SWCNTs or MWCNTs is similar to the G-band observed in graphite, with one peak around 1580 cm^{-1} [47].

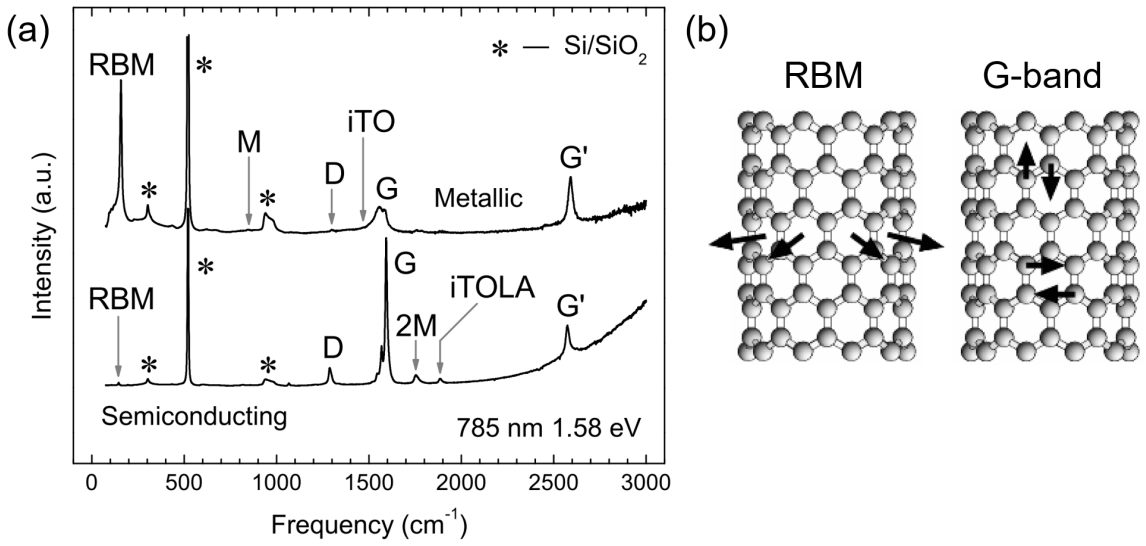

Figure 2.2: (a) Raman spectra of a metallic (top) and a semiconducting (bottom) SWCNT [44]. (b) Schematic of atomic vibration of the RBM and the G-band [45].

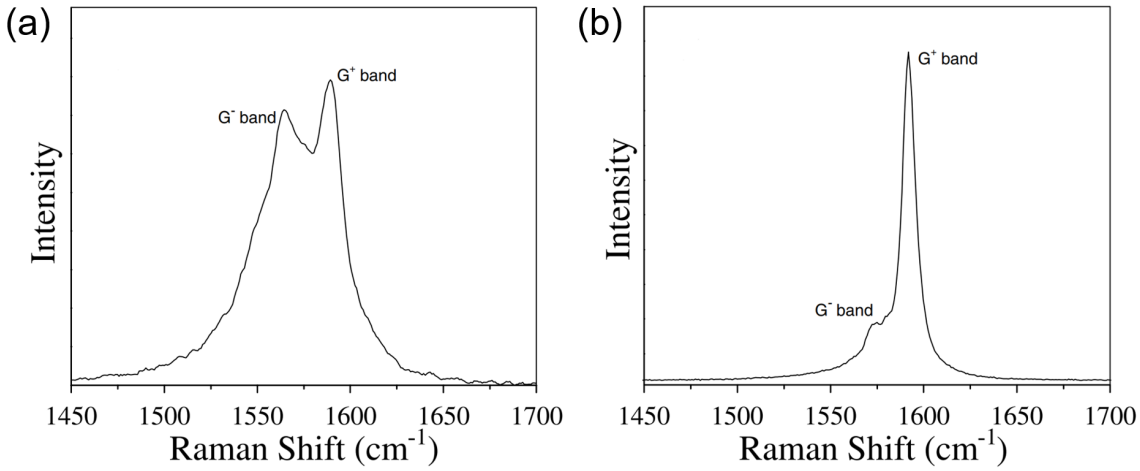

Figure 2.3: G-band features in Raman spectra of a (a) metallic and a (b) semiconducting SWCNT [46].

Because of the unique 1D structure, the excitation of G-band vibration along CNTs longitudinal axis has a strong dependence on the linear polarization direction of the excitation source [46]. Lei et al. conducted polarized Raman spectroscopy experiment on individual SWCNTs (Figure 2.4(a)) [46]. They found that the intensity of the G-band is a function of the angle of polarization. Figure 2.4(b) shows their Raman spectra at different angles of laser polarization with respect to the longitudinal axis of the CNT. The peaks (G^+ and G^-) of the G band show maximum intensity when the incident light is parallel to the longitudinal axis and minimum when perpendicular to the longitudinal axis.

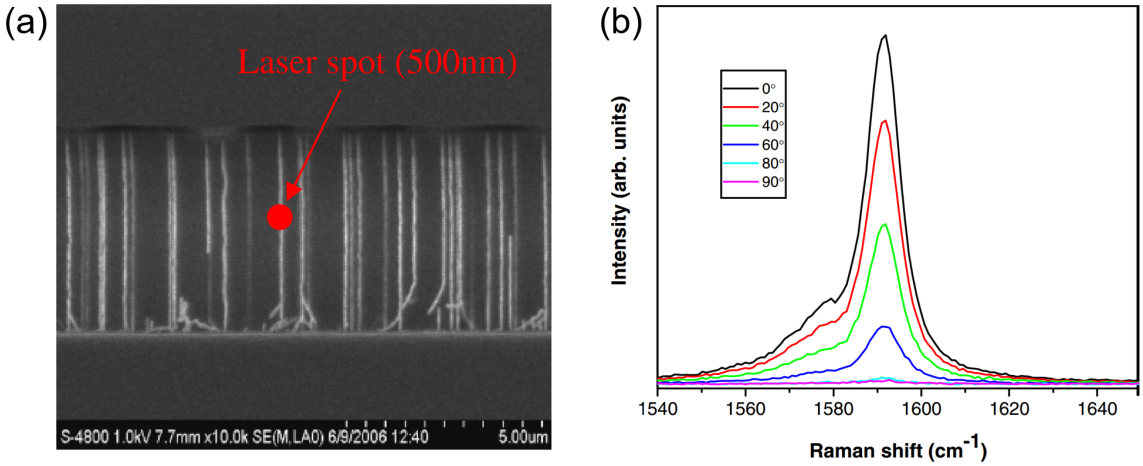

Figure 2.4: (a) SEM image of aligned SWCNTs where red dot indicates laser spot with 0.5 μm in diameter. (b) Polarized Raman spectra of the SWCNT in (a) showing G-band intensity as function of polarization angles (0^o corresponds to the longitudinal direction) [46].

Therefore, the intensities of the G-band peaks serve as a probe for the degree of alignment of CNT (in the composite). Several prior studies have proven the validity of this method by taking polarized Raman spectra on cured composite samples [14, 38]. Figure 2.5 shows the polarized Raman spectra of SWCNT-NaDDBS/PEI composite at different polarization angles [38]. Just like the spectra of the individual SWCNT, the Raman signals are strongest when incident light is polarized parallel to

the longitudinal axis and are suppressed when light is polarized perpendicularly.

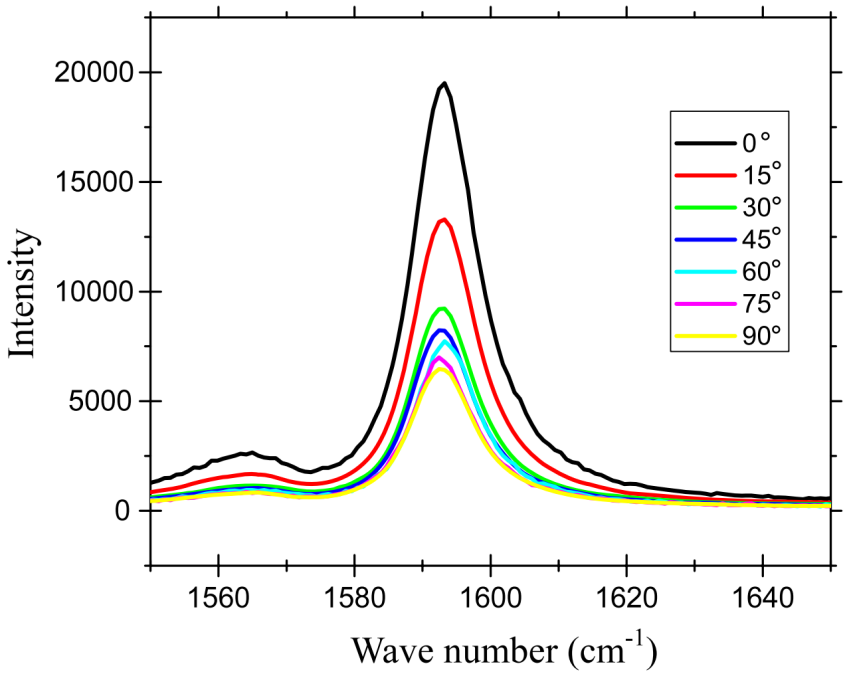

Figure 2.5: Polarized Raman spectra of SWNTNaDDBS/PEI composites at different polarization angles. 0o corresponds to the intended alignment direction [38].

Notice the Raman spectra in Figure 2.4(b) and 2.5 are more like the shape of semiconducting CNTs. There are two reasons: 1) The G-band for semiconducting CNTs has a much higher intensity than that of metallic ones, as seen in Figure 2.2(a). So the G-band shape from metallic CNTs are overwhelmed by that from semiconducting CNTs. 2) Commercially available CNTs typical consist of a large portion of semiconducting CNTs. Because of that, an implicit assumption is made that metallic CNTs and semiconducting CNTs have an equal ability to align. And their amount ratio is consistent from the same supplier. In the literature, the term G-band intensity usually refers to the intensity of the G^+-band. This convention is used throughout the thesis.

2.2 Experimental

2.2.1 Materials

2.2.1.1 CNT

In this research, high purity (over 90%) SWCNTs are used and no chemical modifications are made to the CNT surfaces (pristine CNTs). The CNTs were produced by an electric arc discharge method (P2-SWCNT, supplied by Carbon solutions, Inc.). The ratio of metallic tubes to semiconducting tubes is roughly 1:3. They have an average diameter of 1.4 nm and a length ranges from 0.5-3 μm. This SWCNT is used throughout the thesis unless otherwise specified.

2.2.1.2 Polymer

Two CNT/polymer systems have been studied:

CNT/EPON 828 EPON 828 is a difunctional bisphenol A/epichlorohydrin (DGEBA) liquid epoxy resin (thermoset) from Miller-Stephenson Chemical Company. It has a viscosity of about 12 Pa·s at 25 ^{o}C. The CNT/EPON 828 mixture is used for real-time experiments.

CNT-PSS/PVA The polystyrene sulfonate (PSS) surfactant (434574-100G, average Mw ∼1,000,000) is supplied by Sigma-Aldrich. The polyvinyl alcohol (PVA) matrix (10851-250G, average Mw ∼195,000) is also from Sigma-Aldrich. The CNT-PSS/PVA film is fabricated at the beginning of the study to test the methodology.

2.2.2 Dispersion

Different dispersion strategies were used in this study. In CNT-PSS/PVA, PSS is added as a surfactant to help the dispersion of water insoluble CNTs in PVA matrix. To prepare the CNT-PSS/PVA solution, the CNT powder is loaded into

the test-tube first and then the corresponding amount of PSS solution, PVA solution and deionized water is added. The mixer is sonicated for 2-4 hours for dispersion (depending on PVA concentrations) using an ultrasonic bath (M2800 110W 40kHz from Bransonic). The amount of CNT and PSS are kept at a constant 1:2 ratio to ensure an adequate amount of surfactant (Recipe from Prof. Nicholas Kotov from University of Michigan). Good dispersion of CNTs is confirmed by microscopy or UV-Vis spectroscopy. UV-Vis spectroscopy is commonly used to monitor the dispersion of CNTs in aqueous solutions [48]. It relies on the observation that only individual CNTs fluoresce (when metallic CNTs quenching semiconducting ones). Thus better dispersion gives a higher UV-Vis signal because more individual CNTs are separated from agglomerates or bundles. In our experiment, dispersion is controlled by sonication. Longer sonication time (constant power) corresponds to higher total sonication energy applied to the CNT/polymer system. Grossiord et al. found the peak intensity from the UV-Vis spectra increases with increasing sonication energy at the beginning and later reaches a plateau. The plateau was referred to as maximum exfoliation of CNTs, namely optimal dispersion of CNTs. Beyond the plateau, further sonication is expected to cause damage to the CNTs. The optimal conditions were determined by my colleague Dr. Wesley Chapkin [49].

In CNT/EPON 828 suspension, the CNT can be dispersed uniformly without additional surfactants. The viscosity of the suspension holds the CNTs in place and inhibits random motion, preventing the formation of agglomerates. CNTs and the epoxy resin are mixed in a beaker, and sonicated for 20 minutes (total energy of 360 kJ) using a horn sonicator (Q700 supplied by QSonica) with a 0.5-inch tip at an amplitude of 30.

This mixing strategy was generated by Prof. Lawrence Drzal from Michigan State University.

Table 2.1 summarizes the composite materials used in this thesis. For both

polymer systems, the CNT concentration was 0.01% throughout the study (discussed in 2.3). The dispersed CNT/EPON 828 mixture is used in our real-time Raman experiments. The CNT-PSS/PVA solution is used to fabricate films (contains 0.2 wt% CNT unless otherwise specified) by evaporating water (details in the corresponding later chapters) to test the methodology.

Table 2.1: Summary of materials used in this work.

Composite	**SWCNT-PSS/PVA**	**SWCNT/EPON 828**
CNT wt%	0.01	0.01
Polymer	PSS: 434574-100G, average Mw ∼1,000,000 PVA: 10851-250G, average Mw ∼195,000	EPON 828: difunctional bisphenol A/epichlorohydrin (DGEBA)
Dispersion method	Surfactant, sonication	Sonication
Viscosity at 25 ^{o}C	10^{-3} Pa·s for 20 mg/mL PVA (depends on PVA wt%)	12 Pa·s
Film preparation	Heated to evaporate water	

2.2.3 Raman Spectroscopy

A Raman spectrometer is integrated with different external forces, i.e. electric field, magnetic field, shear force, as shown in Figure 2.6. We collaborated with Prof. Kieffer (Customized Raman spectrometer) and Prof. Lahann (Witec Confocal Raman spectrometer). A green light laser of 532-nm wavelength is used as the excitation source. Both incident and scattered laser light can be polarized (two waveplates). Samples (either solution or film) are placed on a XY stage with laser light coming vertically from the top. The laser is focused through a 10x objective lens at a powder of 5±0.05 mW, with a maximal focal length of 14 mm. For film measurement, the laser is focused at the middle of the film thickness . The focal depth for real-time solution characterization is 400 mm from the surface of the sample (determined empirically). Back scattered light is collected for Raman analysis. The integration time for each spectrum is 5 seconds, unless otherwise specified.

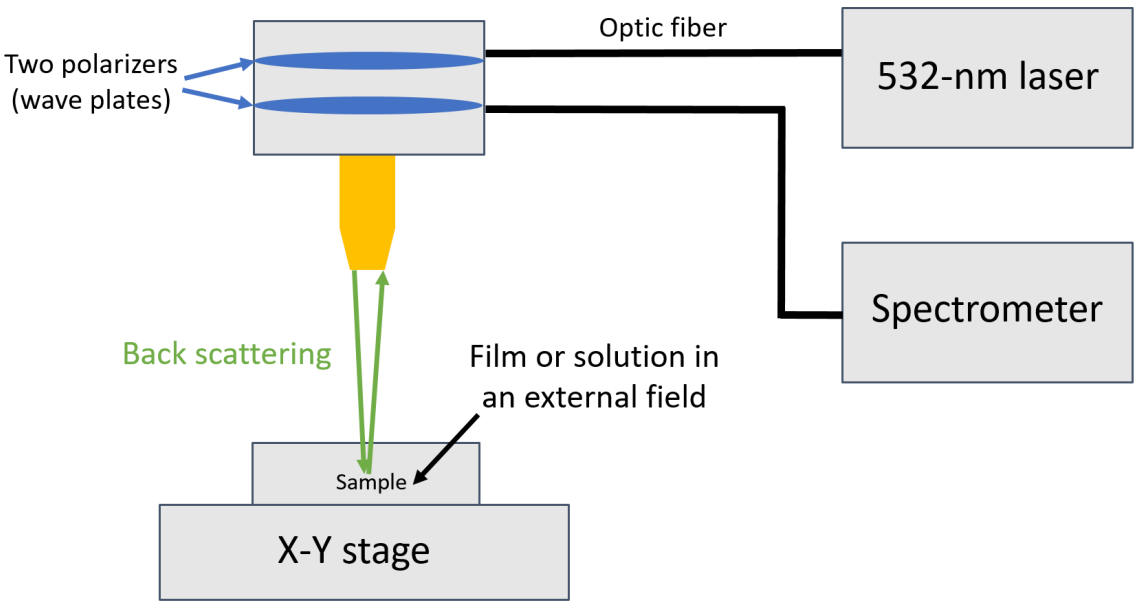

Figure 2.6: Schematic of polarized Raman spectroscopy setup.

For *in situ* measurement, an external force (electromagnetic field or shear force) is applied to induce alignment while polarized Raman spectra are being taken. Two wave plates are used to polarize both the incident and the scattered light. The polarizations are denoted by HH or VV, where the first letter refers to the polarization of the incident light and the second letter denotes the scattered light. The H polarization is parallel to the direction of the applied force and V is perpendicular to it. The real-time Raman spectra are collected at the HH polarization during the course of alignment and a few at the VV polarization at the end of alignment, to calculate the HH/VV ratio. For CNT-PSS/PVA films, this ratio is calculated by H/V. This is because the PVA composite film is too thin ($\sim$100 μm) so only incident light is polarized to maximize the Raman signal.

2.3 Results and Discussion

2.3.1 Raman Spectra

Figure 2.7 shows the Raman spectrum of our CNT powder, with the major peaks labeled. The shape of the G-band is similar to semiconducting tubes in Figure 2.3(a), which agrees with the supplier's claim that a approximately ∼two-thirds of the sample is semiconducting tubes.

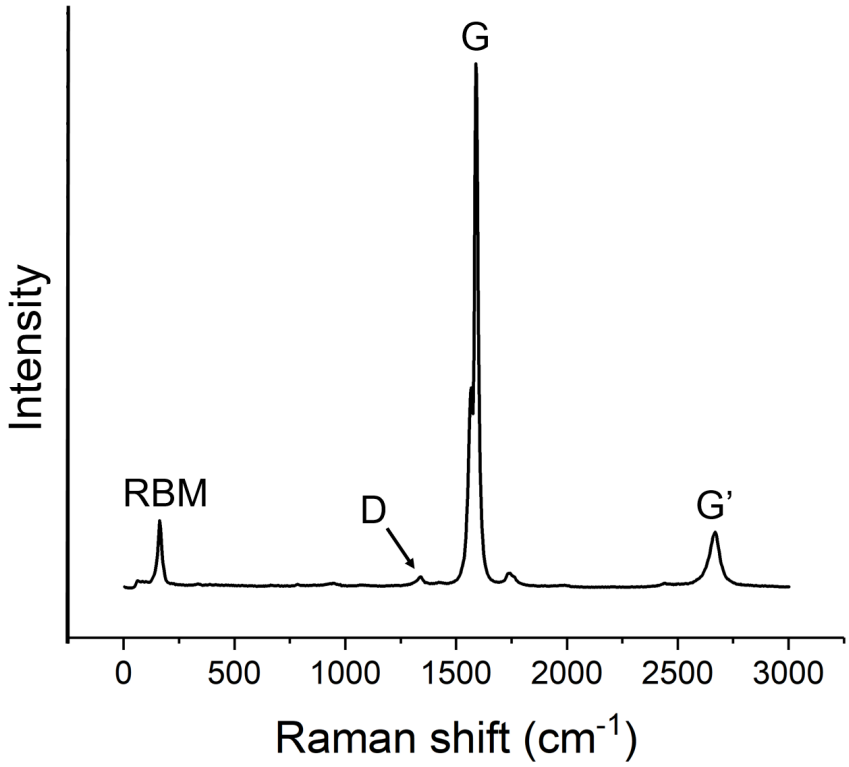

Figure 2.7: Raman spectrum of our SWCNT powder.

When mixed with EPON 828, more spectral features (bands) appear on the Raman spectrum. One epoxy peak, at around 1610 cm^{-1}, overlaps with the CNT G-band (Figure 2.8). The shape of this combined spectra features depends on the CNT loading as the G-band intensity is proportional to the amount of CNT in the focal area. Figure 2.8 shows the Raman spectra of CNT/EPON 828 mixture at loadings of 0.005 and 0.01 wt%. On one hand, high CNT loading is desired to boost

signal-to-noise ratio. On the other hand, high loading generally lowers the dispersion quality and increases the opaqueness of the CNT/EPON 828 mixture that decreases the penetration depth of the laser. A CNT loading of 0.01 wt% is determined based on this trade-off and is used throughout this thesis, unless otherwise specified.

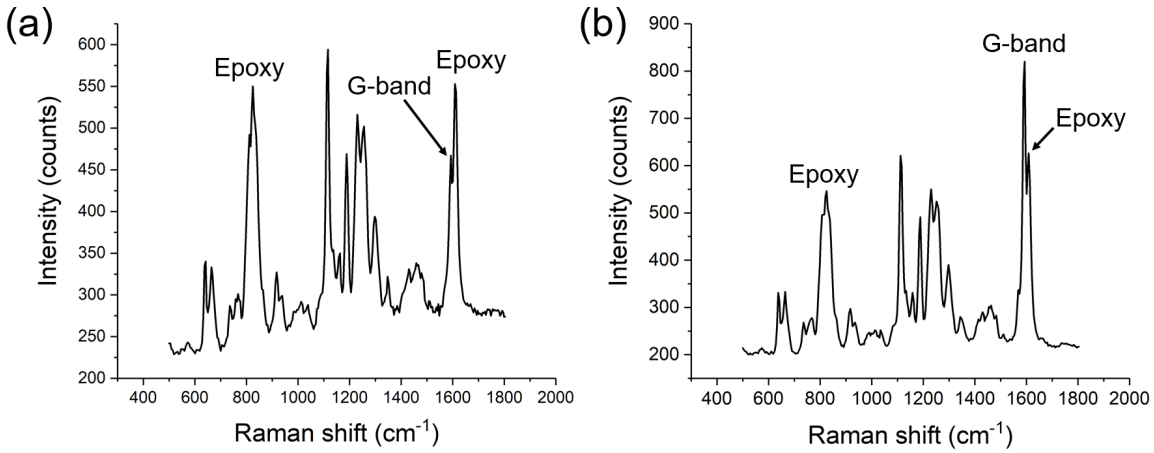

Figure 2.8: Raman spectra of CNT/EPON 828 mixture at the loading of 0.005 (a) and 0.01 wt% (b). The G-band and two epoxy peaks (824 and 1610 cm^{-1}) are labeled.

The epoxy polymer chains are assumed to not align under the applied field and are always randomly oriented (see Appendix B). Therefore, the epoxy peak at 824 cm^{-1} is used as an indicator of the fluctuation of the system. Detailed data processing methods are described below.

Figure 2.9 shows a Raman spectrum of the CNT-PSS/PVA film. It is similar to the spectrum of the CNT powder, except for an additional PVA peak at around 2900 cm^{-1}.

Figure 2.10 shows typical G-band curves at HH and VV polarization for unaligned (a) and aligned (b) CNT samples. The samples in this case is CNT/EPON 828 mixture and similar shapes have been observed in the CNT-PSS/PVA film as well (at H and V polarizations). No obvious changes are observed for the unaligned sample. For the aligned sample, the G-band intensity at HH polarization is significantly higher

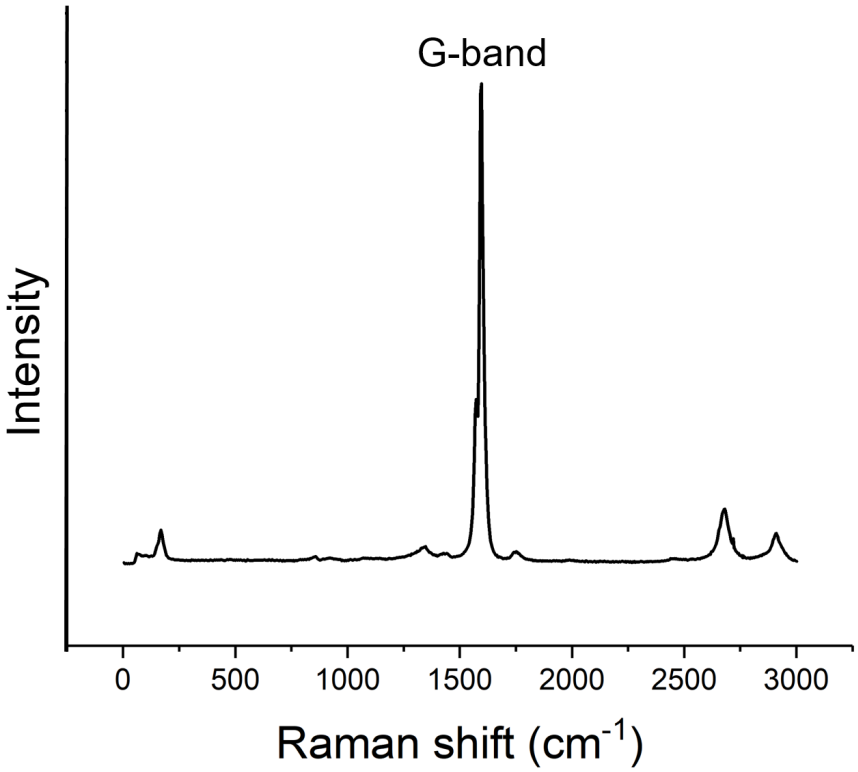

Figure 2.9: Raman spectrum of CNT-PSS/PVA film.

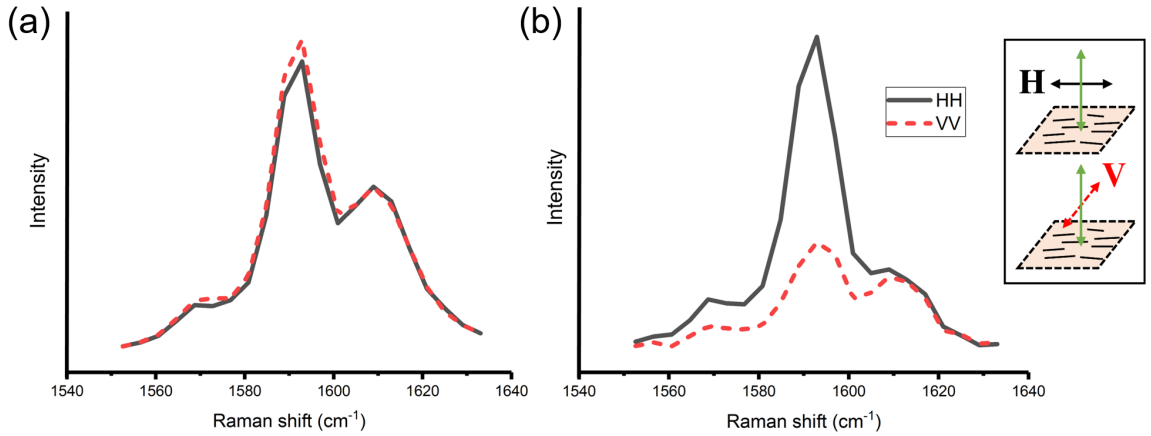

Figure 2.10: G-band curves collected at HH and VV direction for unaligned (a) and aligned (b) CNT samples. The inset [49] demonstrates the schematic of the polarization directions.

than that of the VV direction. The inset [49] demonstrates that the H polarization is parallel to the alignment direction while V is in the perpendicular direction.

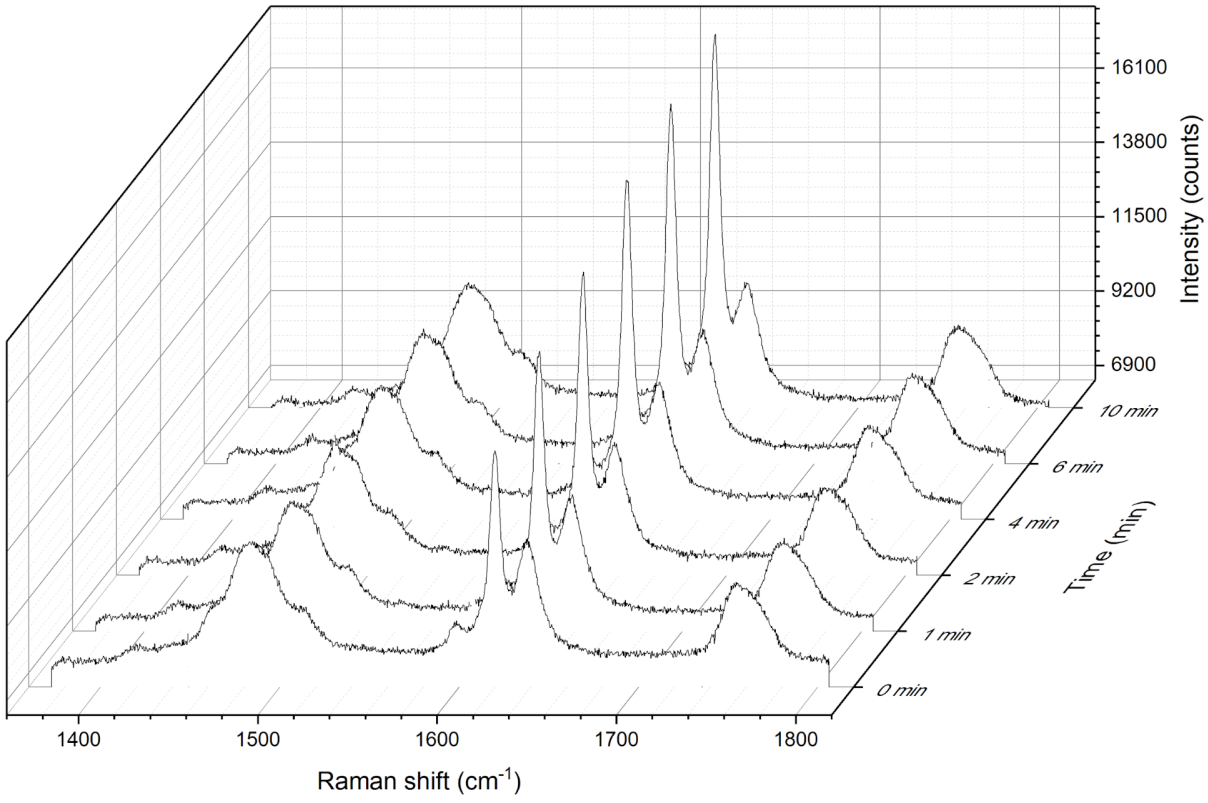

Figure 2.11: Serial Raman spectra are collected over time for the real-time experiment.

2.3.2 Spectra Processing and Analysis

For real-time experiments, we collect a series of Raman spectra over time as shown in Figure 2.11. These spectra are then processed and analyzed using the program *WITec Project*.

To compare experiments of different samples, the G-band intensities (1590 cm^{-1}) are normalized to the epoxy peak at 824 cm^{-1}, which remains approximately constant

during an experiment. It has been shown deconvolution of G-band from the nearby epoxy peak (1610 cm^{-1}) is not necessary [49].

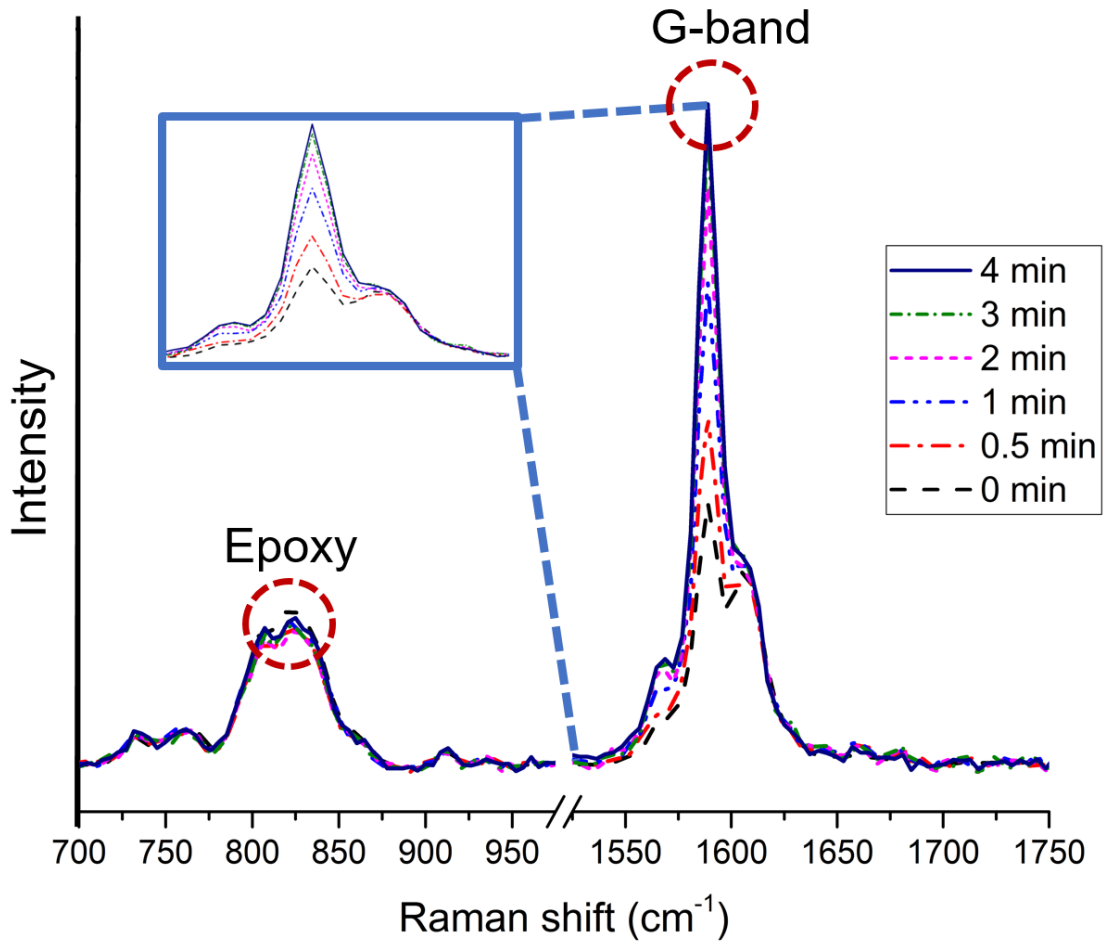

Figure 2.12: The intensities of the G-band (1590 cm^{-1}) and the epoxy (824 cm^{-1}) are extracted from serial Raman spectra. Inset shows a zoom-in view of the G-band curves.

The normalized G-band intensity (I_{norm}) is calculated according to Equation 2.1:

$$I_{norm} = \frac{I_t(CNT_{1590})/I_t(Epoxy_{824})}{I_0(CNT_{1590})/I_0(Epoxy_{824})} \tag{2.1}$$

Where $I_0(CNT_{1590})$ and $I_0(Epoxy_{824})$ are the initial intensities of the G-band and the epoxy at $t = 0$ min, and $I_t(CNT_{1590})$ and $I_t(Epoxy_{824})$ are the intensities at any given time t during the experiment.

An example of normalized G-band curve at HH polarization is shown in Figure 2.13. As CNTs begin to orient in the direction of the applied field, the normalized G-band intensity normally increases over time at HH polarization. In this thesis, unless otherwise specified, "G-band intensity" refers to normalized G-band intensity at HH polarization.

The HH G-band curve can be fitted by an an exponential function:

$$I_{norm} = 1 + A - A \cdot exp(-t/\tau) \tag{2.2}$$

Where A is a constant fitting parameter, t is the corresponding time step for the normalized intensity I_{norm}, and τ is another fitting parameter, the time constant.

This curve fitting is performed in *Origin* using the *Orthogonal Distance Regression method*. The exponential fit gives an asymptotic value that can be recognized as the G-band intensity at the steady-state plateau. For a real-time experiment, this value corresponds to the highest G-band intensity at the HH polarization. A few VV spectra are collected at the end of the alignment (when the plateau is reached) 2.13. Associated G-band intensities are also normalized according to Equation 2.1 and averaged. The ratio of the normalized G-band intensity at HH and VV polarizations are calculated, as is commonly used as a measure of the degree of alignment. In Figure 2.13, the normalized G-band intensity at VV polarizaion is below 1 as less CNTs are oriented in VV direction. If we collect real-time VV spectra, the G-band intensity shows a decreasing trend (Figure 2.14). Thus the HH/VV ratio is larger than 1 when CNTs are aligned. The larger the ratio, the greater the alignment. It is worth noting the polarization angles need to be manually set (by rotating waveplates), so the spectra cannot be collected at both HH and VV polarizations simultaneously.

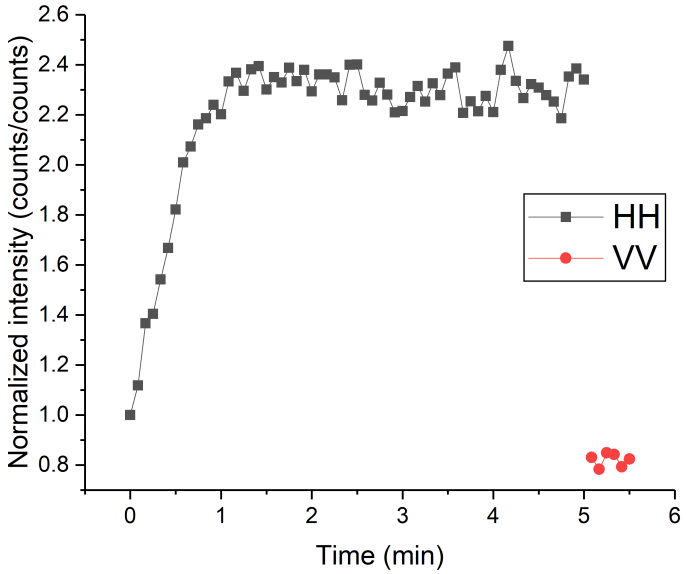

Figure 2.13: Normalized G-band intensities over time from spectra collected at HH polarization (black square). Six VV spectra are collected at the end of alignment and G-band intensities (red circle) are extracted and averaged, to collect the HH/VV ratio.

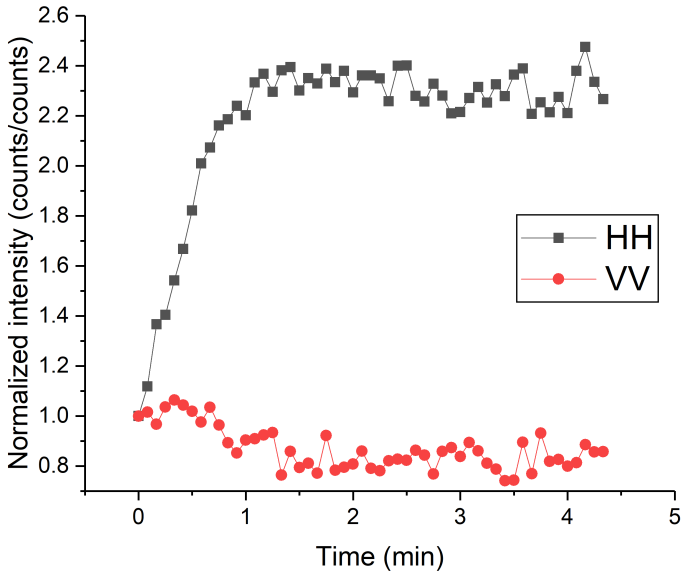

Figure 2.14: Normalized G-band intensities over time from spectra collected at HH (black square) and VV (red circle) polarizations (two separate experiments). G-band intensity decreases in VV direction.

2.4 Conclusion

An *in situ* Raman spectroscopy has been developed to measure CNT alignment in real time. We used CNT/EPON 828 mixture for real-time study and fabricated CNT-PSS/PVA film to test the methodology. The experimental details and spectral data handling are described. In the following chapters, this technique is applied to study the alignment kinetics under different external forces. Specifically, electric field, magnetic field and shear force.

CHAPTER III

Electric Field Alignment

3.1 Introduction

Electric field alignment is intriguing because the experimental setup is simple and easy to control. CNTs are highly susceptible to electric field and are aligned in the direction of the applied field. The manipulation of CNT under electric field can be summarized as three separate processes [7, 18, 19]. 1) The application of the electric field polarizes the CNT and induces a dipole moment. This leads to a torque acting on the CNTs and tending to orient them in the field direction. 2) The aggregated charges at two ends of CNTs produce attraction and repulsion forces which drives CNT to move closer to each other. 3) CNTs start to become connected to each other and form bundles by attraction between the aggregated charges or by Van Der Waals attraction. Figure 3.1 shows a schematic of the three steps evolution of CNT alignment in electric field [18]. Gradually these bundles grow thicker and a connected CNT network structure forms. The latter two processes would disrupt the dispersion and thus degrade the properties [18, 19]. Therefore, to achieve better mechanical properties of the final product of composite, it is important to make sure the alignment is completed while the migration is minimized. The migration can be captured and characterized through optical microscopy [18, 19] due to the large size of these bundles.

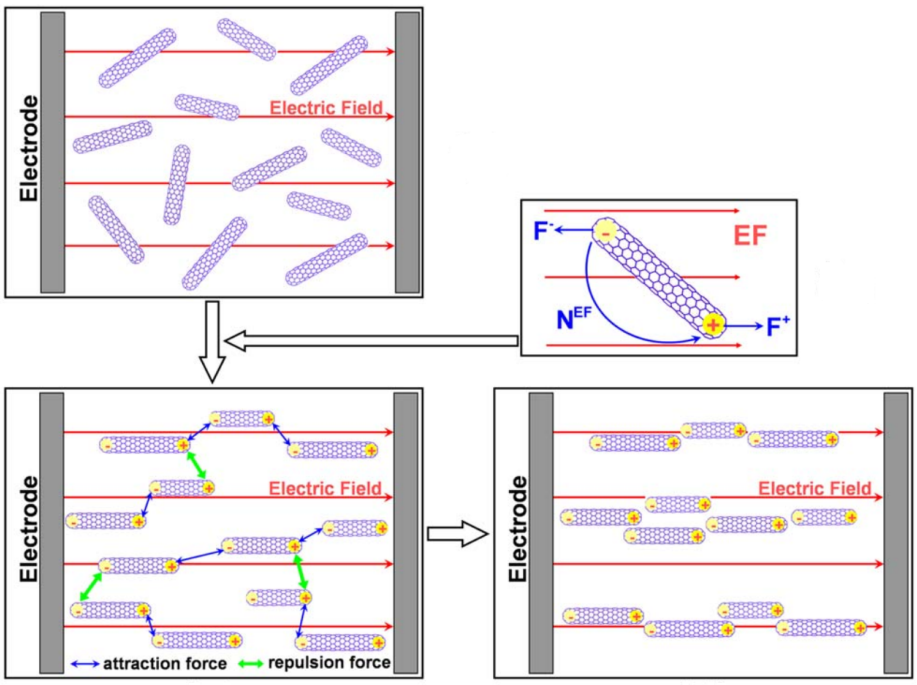

Figure 3.1: Schematic of the three-step CNT aligning process in electric field [18].

The morphologies of CNT alignment are different for direct current (DC) and alternating current (AC) fields. More CNT migration and thicker CNT bundles are observed for DC field while more uniform alignment and thinner bundles are seen in AC field. In DC field, CNTs migrate towards one end of the electric field and a CNT network gradually forms from that end. But in AC field, translational migration of CNTs does not occur and the CNT network forms from both ends. The CNT network is less uniform in DC field as the migration creates heterogeneity. Also, CNT bundles are thicker due to a higher possibility of CNTs coming across each other and forming bundles. Figure 3.2 shows optical micrographs of MWCNT/epoxy composites during curing in DC field (a) and AC field (b) of same field strength [7].

The dynamic behavior of CNTs in a polymer suspension under the influence of an electric field is complex. Both electrophoresis and dielectrophoresis of CNT can occur in electric field alignment [7, 18, 19], resulting in the extensive migration of CNT in the DC field. On one hand, surface charged CNTs move to the electrode

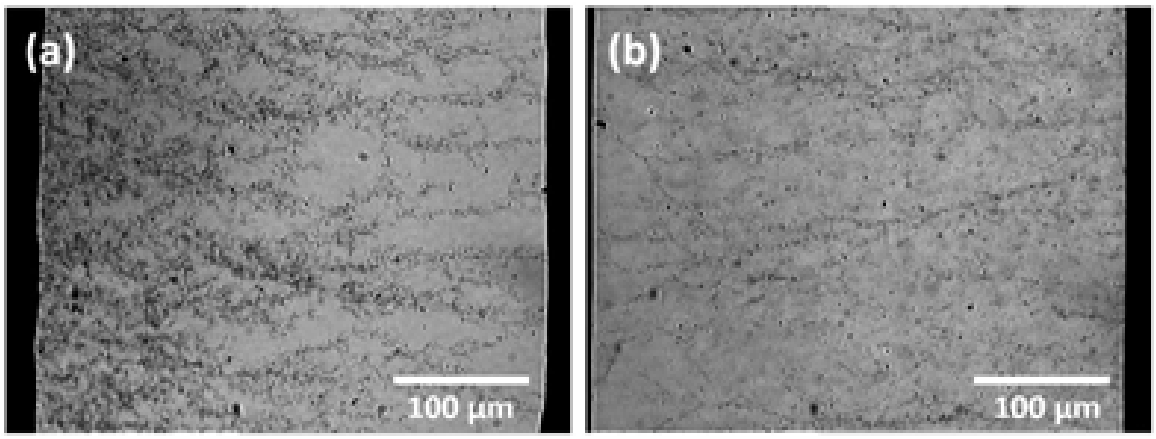

Figure 3.2: Optical micrographs of MWCNT (0.01 wt%)/epoxy composite at a time of 240 min during curing at 80 ^{o}C in DC field (a) and AC field (b) of 100 V/cm [7].

of the opposite sign due to the electrophoresis of CNT. For example, Martin et al. observed that CNTs moved towards the anode in epoxy suspension [7]. When CNTs moved close enough to the anode, charge transfer occurs and they adsorb onto the anode. The tips of CNTs connected to the anode then serve as sources of high field strength and location for further adsorption of other CNTs. Thus the CNT network evolved from one-side of the electric field (CNT network is denser near the left-side anode in Figure 2(a)). The surface charges result from CNT-matrix interaction or from charged particles in surfactants [50, 51]. Dielectrophoresis occurs purely due to the aggregated charges at two ends induced by the electric field instead of the charges present on the tube surface. CNT migration does not occur in AC field because of the continuous flipping of the field direction. Bundle forming is attributed to coulombic attraction between aggregated charges at two ends and the Van Der Waals attraction between tube surfaces. AC field is used throughout this thesis to induce uniform alignment.

3.2 Experimental

3.2.1 Film Preparation

To prepare an electrically-aligned CNT-PSS/PVA film, 2ml of CNT-PSS/PVA suspension is poured into the middle of the two copper electrodes in a petri-dish. The AC signal (sin wave) is first generated by a function generator (Agilent 33500B, 30 MHz) and then amplified by a high-voltage power amplifier (Trek Model 2220) before they reach the electrodes. The voltage gain is fixed at a ratio of 200 V/V, i.e. 1 V generated by the function generator gives a 200 V output of the amplifier.

The petri-dish is placed on a hotplate (SP131325 supplied by Thermo Scientific) while kept at 90 ^{o}C for 45 minutes to evaporate water (Figure 3.3). Electric field is applied during evaporation. Unaligned films are prepared through exactly same process except electric field turned off.

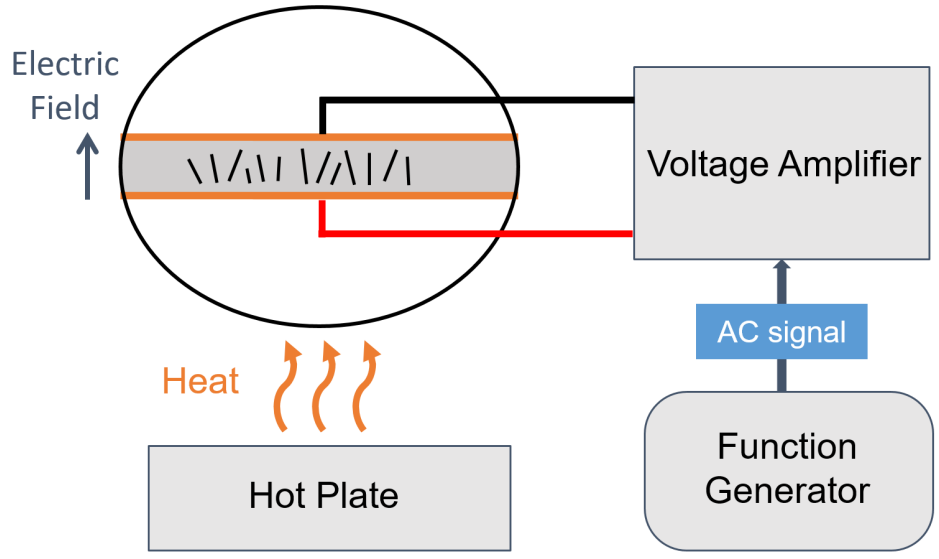

Figure 3.3: CNT-PSS/PVA solution heated by a hotplate while AC field is on.

3.2.2 Real-time Experiment

The CNT/EPON 828 mixture is placed in a cuvette (10 mm x 10 mm cross section) with copper plates on each side (Figure 3.4). The AC field is generated as described above. The polarized laser light enters the sample from top and focuses at a depth of 400 mm (back scattering) as described in detail in Chapter II.

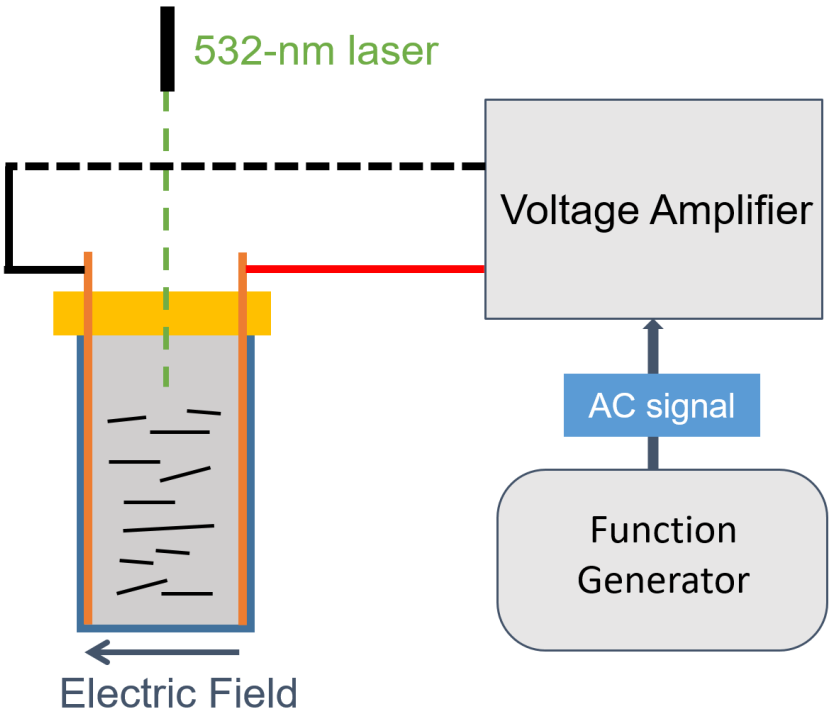

Figure 3.4: Real-time monitoring of CNT alignment changes under AC field through polarized Raman spectroscopy.

3.3 Results and Discussion

The CNT-PSS/PVA composite films is made by the procedure described above. Polarized Raman spectra show no change in G-band intensity for an unaligned sample (Figure 3.5(a)) while in an electrically-aligned sample (Figure 3.5(b)), G-band intensity in the electric field direction (H) is higher than that of the perpendicular direction (V). The G-band intensity ratio, H/V is 1.03 for unaligned sample and 3.16 for aligned

one. This indicates CNTs are preferentially aligned in the direction of the electric field.

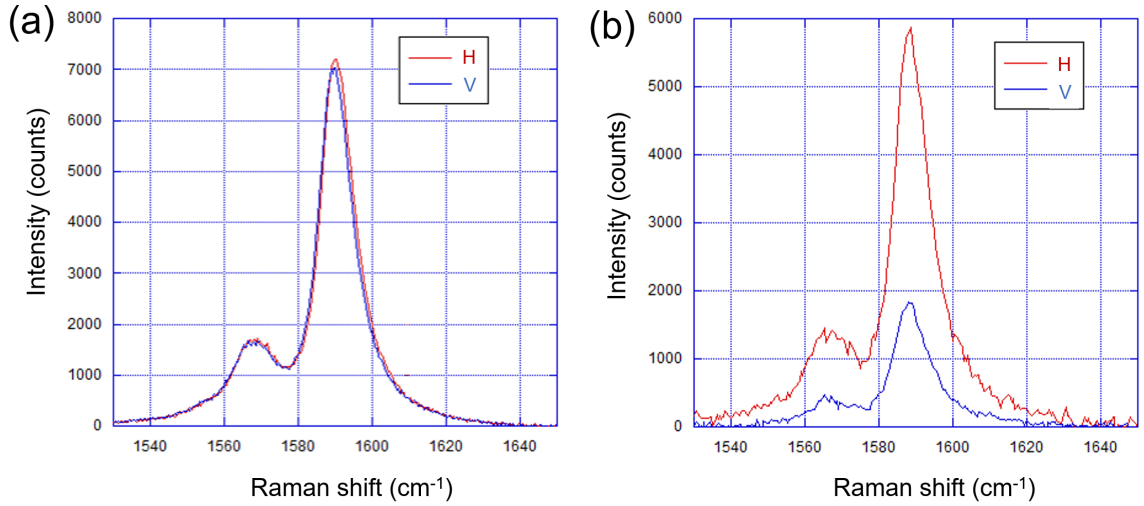

Figure 3.5: G-band curves of random (a) and electrically aligned (b) CNT-PSS/PVA film (300 V/cm, 1 kHz).

Polarized real-time Raman spectroscopy is applied on CNT/EPON 828 mixture for kinetics study. The G-band intensities, from polarized Raman spectra, are normalized (described in Chapter II) and plotted over time (Figure 3.6). The growth rate of G-band intensity is largest at the beginning and it gradually decreases to zero where the intensity reaches a steady-state plateau. This evolution of the G-band intensity confirmed the validity of the proposed real-time Raman spectroscopy. Increasing the AC field strength increases both the speed and the degree of alignment. Detailed analysis of alignment under electric field has been investigated by my colleague Dr. Wesley Chapkin [49].

3.4 Conclusion

We have demonstrated the ability to make aligned CNT film and to measure the real-time changes of CNT alignment in the AC field. Besides electric field, other

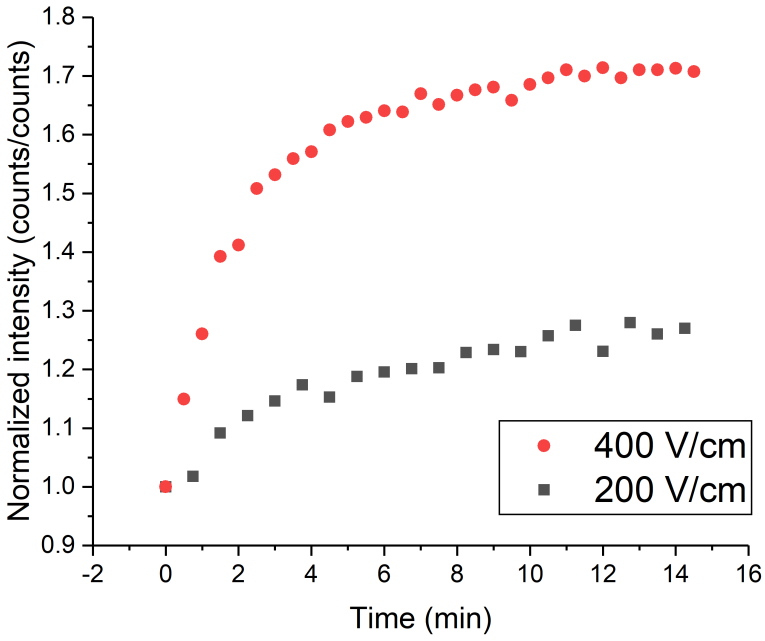

Figure 3.6: Normalized G-band intensities as a function of time for CNT/EPON 828 in AC field strengths of 200 and 400 V at a 7.5 kHz frequency.

external forces have not been well studied, due to the difficulty of setting up the field. However, these fields have their own intriguing properties and potential benefits. The following chapters show our application of this real-time Raman technique to study alignment under magnetic field and shear force.

CHAPTER IV

Magnetic Field Alignment

4.1 Introduction

Magnetic field (especially high field) is more difficult to set up but has the advantage of not touching the materials (in electric field setup, electrodes have to be immersed in the composite solution) and not generating Joule heating. Pristine (chemically unaltered) CNTs usually require a high magnetic field (above 5 T) to induce alignment [24].

It is worth noting that as-synthesized, CNTs typically have a magnetization several orders of magnitude higher than purified CNTs because of the entrapped catalytic nanoparticles. Regardless of whether they are metallic or semiconducting tubes, CNTs are always aligned with tube axis parallel to the direction of the magnetic field due to their unique anisotropic magnetic susceptibility [22, 23]. Metallic tubes are paramagnetic parallel to the tube axis $\chi_{//} > 0$ but diamagnetic perpendicular to the field $\chi_{\perp} < 0$. Therefore, the magnetic anisotropy, $\Delta\chi = \chi_{//} - \chi_{\perp}$, is always greater than zero. Semiconducting CNTs are diamagnetic both parallel ($\chi_{//} < 0$) and perpendicular ($\chi_{\perp} < 0$) to the tube axis. The diamagnetic susceptibility is most negative in the perpendicular direction ($|\chi_{//}| < |\chi_{\perp}|$), making the magnetic anisotropy $\Delta\chi = \chi_{//} - \chi_{\perp} > 0$. The magnetic susceptibilities are summarized in Table 4.1.

Table 4.1: Summary of magnetic susceptibilities of CNTs.

CNT Type	**Parallel** χ_1	**Perpendicular** χ_2	**Anisotropy** $\Delta\chi = \chi_{//} - \chi_{\perp}$
Metallic	$\chi_{//} > 0$	$\chi_{\perp} < 0$	$\Delta\chi > 0$
Semiconducting	$\chi_{//} < 0$	$\chi_{\perp} < 0$	$\Delta\chi > 0$

The introduction of magnetic particles either onto or inside the surface of MWCNTs enable MWCNTs to be aligned at relatively weak magnetic field (below 1 T). This modification is not applied on SWCNTs due to their small sizes and the possibility of destroying surfaces. Correa-Duarte et al. decorated MWCNTs with iron oxide nanoparticles (Figure 4.1(a)) and aligned CNTs at a low field of 0.2 T [25]. Korneva at el. infiltrated MWCNTs with iron oxide particles (Figure 4.1(b)) and achieved alignment at an external magnetic field strength of 0.01 T [26].

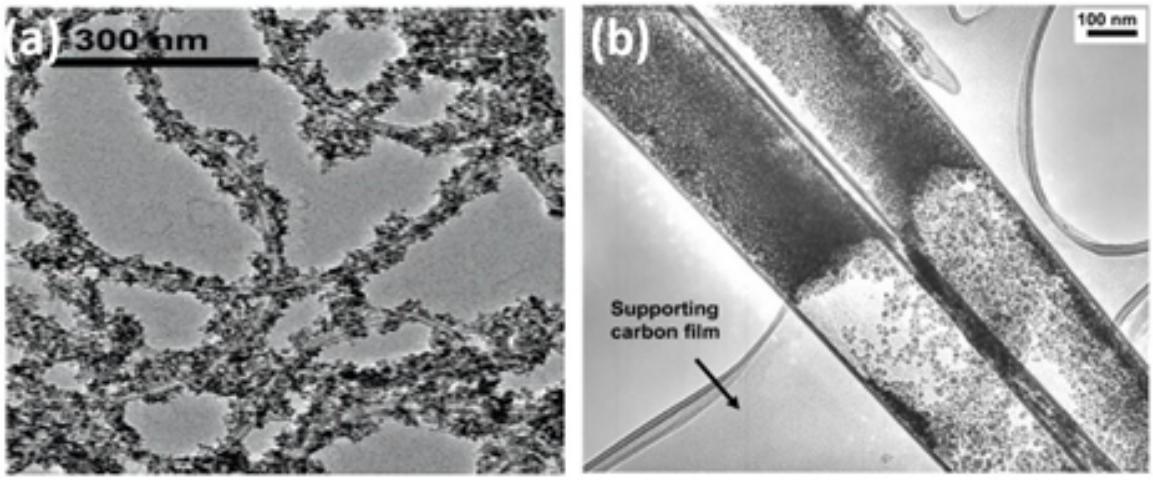

Figure 4.1: TEM images of MWCNTs with iron oxide particles attached on the surface [25] (a) and loaded inside [26] (b).

4.2 Experimental

4.2.1 Film Preparation

To prepare magnetically-aligned CNT-PSS/PVA film, 1.5 ml of CNT-PSS/PVA solution is poured into a custom-made plastic container that surrounded by a magnetic

field. The magnetic field generated by an electromagnet (EMU-75 supplied by Silicon Valley Science Labs) (Figure 4.2(a)). The coils of the magnets are powered by a constant current supply (DPS-175 from Silicon Valley Science Labs) (Figure 4.2(b)). Magnetic field strength is measured using a digital gauss meter (DGM-103, also from Silicon Valley Science Labs).

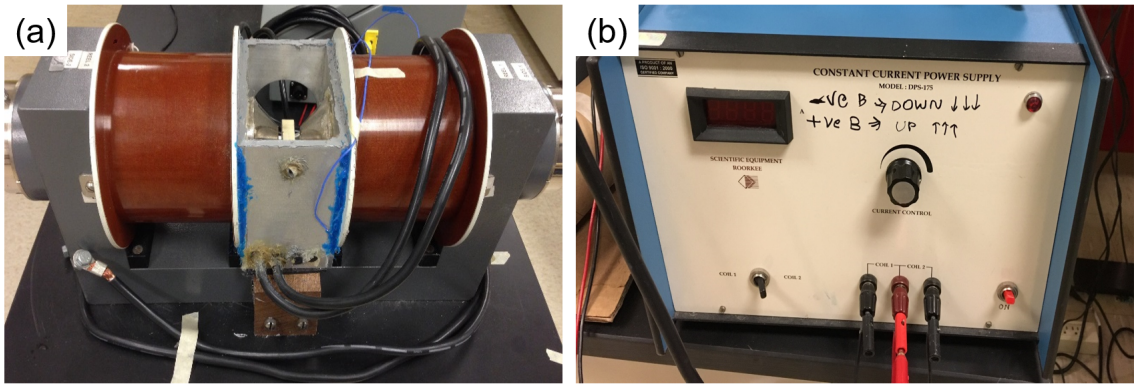

Figure 4.2: Electromagnets (a) and current supply (b).

The solution is maintained at 60 ^{o}C to evaporate the water, for about 45 minutes by an IR heater (Model 4150, Research Inc.)(Figure 4.3). Unaligned films are prepared with magnetic field off for comparison.

4.2.2 Real-time Experiment

For real-time solution measurement, another type of magnetic field is generated by two permanent magnets (e.g. BX088-N52) from K&J Magnetics, Inc. The magnets are attached to a custom-made 3D printed block that enables to slide horizontally so that the magnetic field can be turned on and off easily (Figure 4.4).

The CNT/EPON 828 mixture is placed in a cuvette (10 mm x 10 mm cross section). To apply the magnetic field, the magnets are slid to where the cuvette sits and apply a uniform horizontal field (Figure 4.5). The polarized laser light enters the sample from top and focuses at a depth of 400 mm (back scattering).

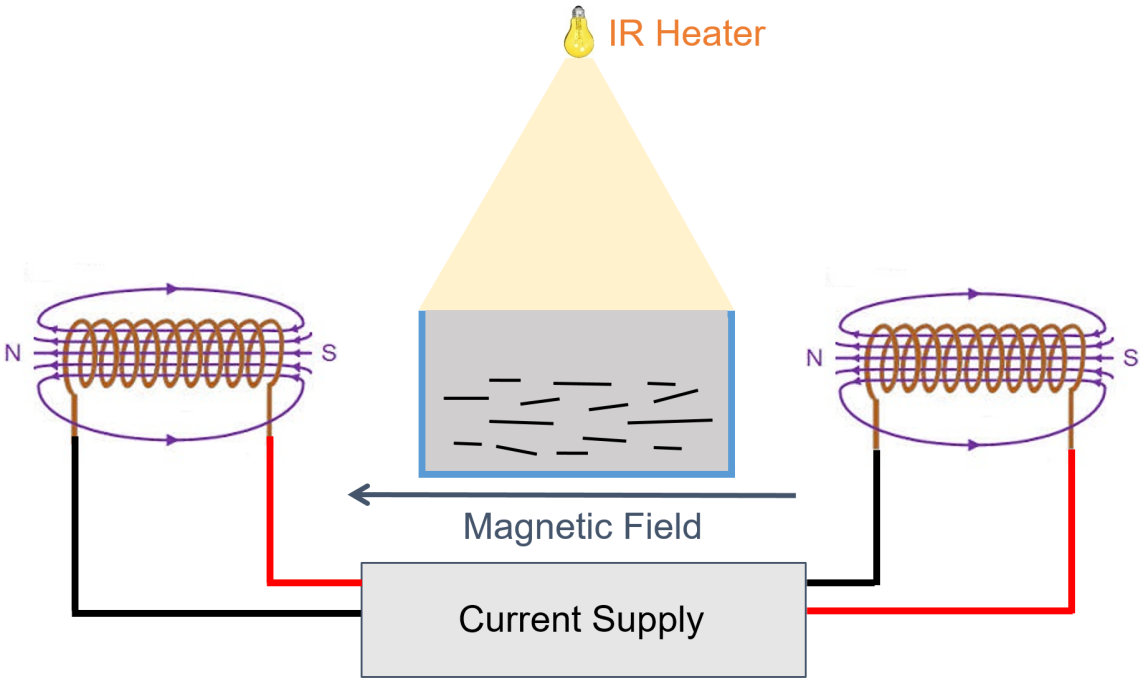

Figure 4.3: CNT-PSS/PVA solution heated by an IR light in a magnetic field.

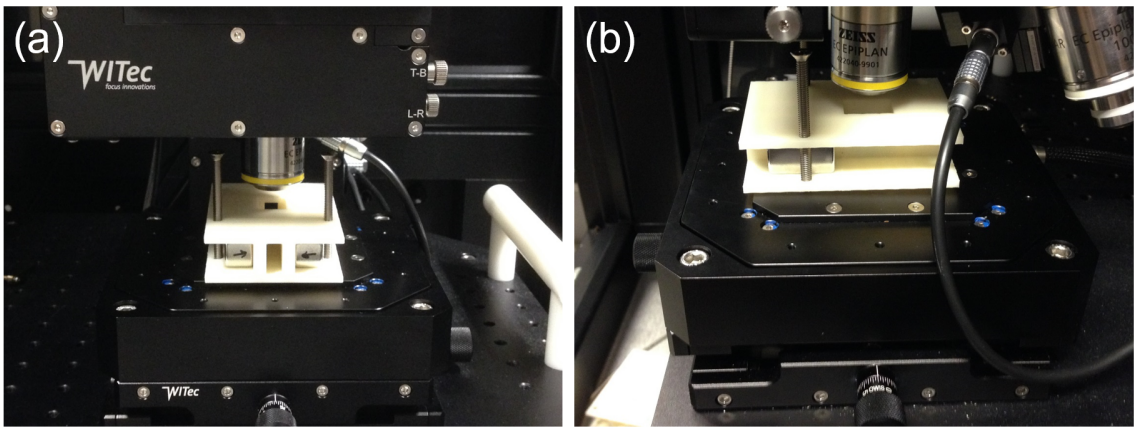

Figure 4.4: Front (a) and side (b) views of sliding permanent magnets in a custom-made 3D printed block.

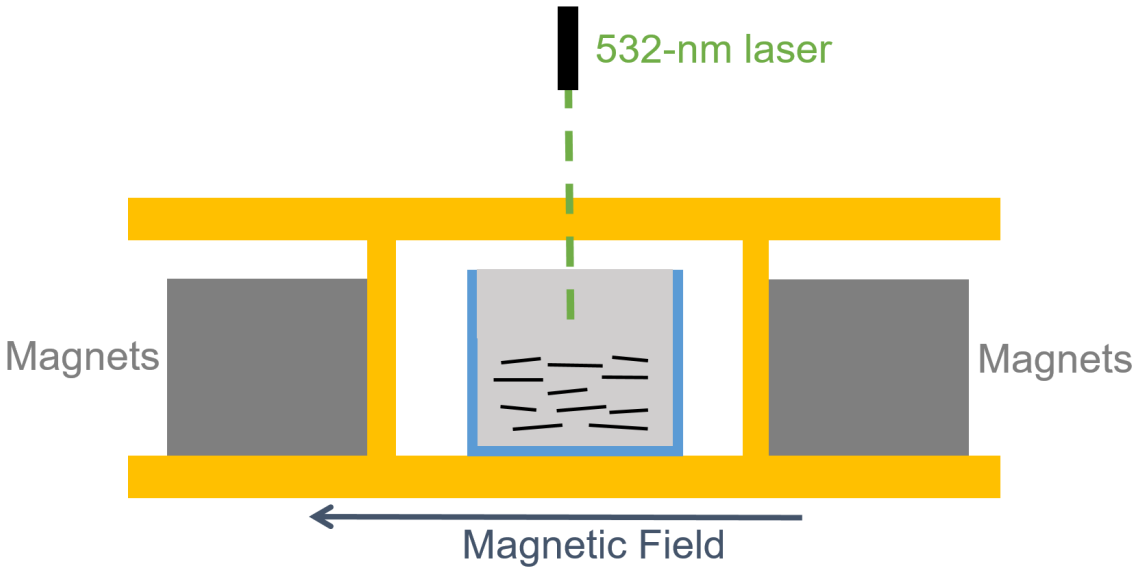

Figure 4.5: Magnetic field is applied by sliding the magnets to where the cuvette sits (front view).

4.3 Results and Discussion

The normalized G-band intensities (normalized to the intensity at polarization 0^o (namely H)) at different polarization angles were measured on magnetically aligned SWCNT-PSS/PVA film, as shown in Figure 4.6. The G-band shows maximum intensity in the magnetic field direction (0^o (H)) and gradually decreases to a minimum at the perpendicular direction (90^o (V)). This anisotropic G-band intensity proves the alignment of CNTs is induced by magnetic field.

Real-time measurement shows a seemingly increasing trend of G-band intensity (Figure 4.7). But the changes are scattered and smaller than those from the electric field experiment.

The scattering of G-band changes may possibly result from translation motion of CNTs. CNTs tend to migrate to the poles of the magnets, which was macroscopically observed both in our experiment and literature [52]. Figure 4.8 shows the translational motion in the CNT/PVA (50 mg/ml) solution (non-dispersed). Large agglomeration

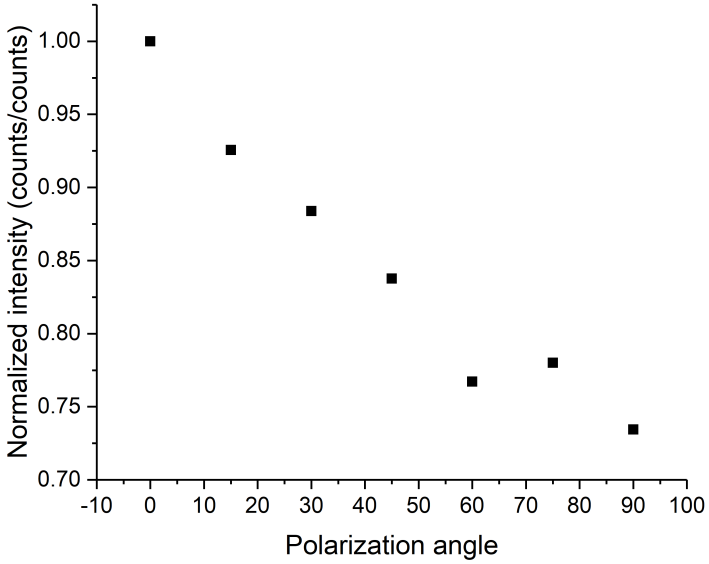

Figure 4.6: Normalized G-band intensities (normalized to the intensity at polarization 0^o (H)) shows a maximum at the magnetic field direction (0^o (H)) and decreases to a minimum at the perpendicular direction (90^o (V)). The CNT-PSS/PVA film is magnetically aligned at a field of 1.2 T.

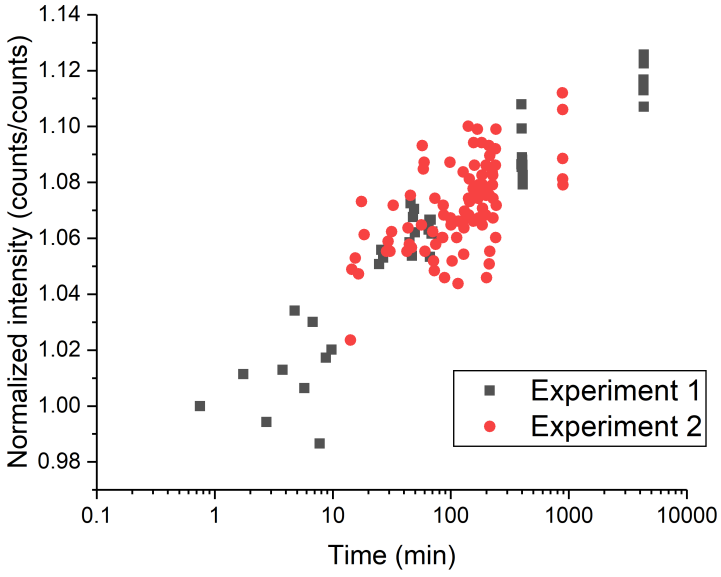

Figure 4.7: Small and scattered changes of normalized G-band intensity in a magnetic field (0.8T). Time is plotted in log scale.

is seen at the edges of the magnet poles when the solution was exposed to a field of 1 T for 20 minutes. The CNT translational motion could lead to CNTs entering and leaving the laser focal area while we are taking the Raman spectra, causing the variations in the amount of CNTs and thus the G-band intensity. This heterogeneity has been observed in film measurement (Appendix C).

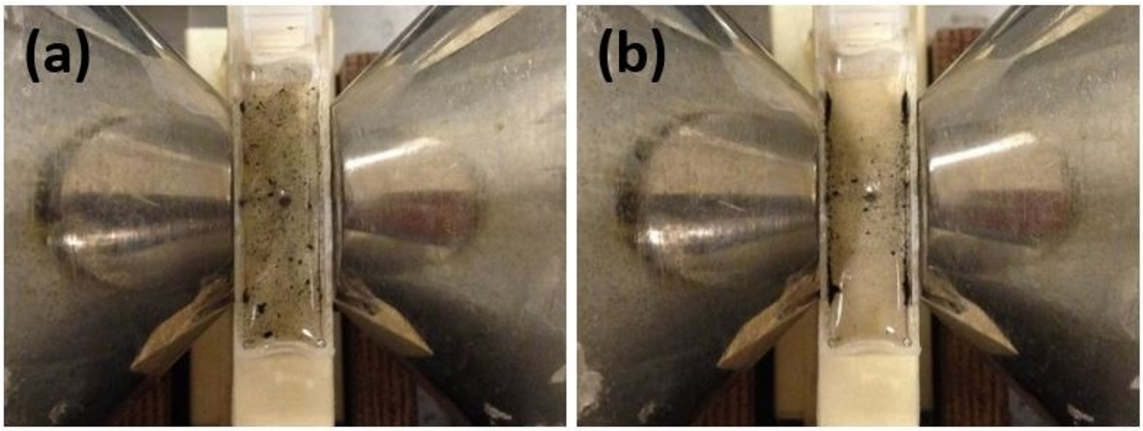

Figure 4.8: CNT in PVA (50mg/ml) under magnetic field of 1 T at time $t = 0$ min (a) and $t = 20$ min (b).

The weak alignment effect is probably due to the low magnetic susceptibility of our SWCNTs and the low field strength. Pristine CNTs have magnetic susceptibility on the order of 10^{-6} emu/g [24]. The values increases to 1-10 emu/g for CNTs containing magnetic catalysts [53]. Decorated or infiltrated CNTs can reach even higher, above 50 emu/g [25, 26].

Kimura et al. proposed a *minimum volume theory*: one necessary condition for the alignment to occur is that the diamagnetic/paramagnetic particle should be large enough to overcome the thermal energy [54]. Alignment will not occur if the particle has a volume smaller than the minimum volume, even if the external field strength is high. Through calculation (Appendix D), the volume of our SWCNTs are 10^{-24} m^3 while the minimum volume required for alignment to occur at 1 T is 10^{-13} m^3, our CNTs being 11 orders smaller. The small changes of G-band intensity might

result from the alignment of a small portion of large CNT bundles or aggregates. In comparison, the literature reported decorated [25] and infiltrated [26] MWCNTs have a volume 3 and 6 orders larger than the calculated minimum volume. Table 4.2 surveys different CNT types and field strengths in magnetic alignment studies in the literature. Pristine CNTs, either SWCNT or MWCNT, generally needs much higher field strength (at least 5 T) than their chemically-treated counterparts.

Table 4.2: A survey of CNT types and magnetic field strengths in the literature.

	CNT Type	**Field Strength (T)**	**Ref.**
Pristine Tubes	SWCNT	15, 25	[55]
	SWCNT, MWCNT	15, 25	[32]
	SWCNT (buckypaper)	7, 26	[27]
	SWCNT (buckypaper)	17.3	[16]
	SWCNT (buckypaper)	19	[23]
	MWCNT	10	[24]
Coated Tubes	Ni-MWCNT	<0.5	[56]
	Fe_2O_3-MWCNT	0.3	[52]
	Fe_2O_3-MWCNT	0.01, 0.03	[26]
	Fe_2O_3-Fe_3O_4-MWCNT	0.2	[25]

Our maximum field strength is 0.8 T for real-time experiment and 1.2 T for aligned film. It has been found that the activation energy of electromagnetic alignment scales with the viscosity of the polymer matrix [49], thus making CNTs much more difficult to align in the epoxy system than in the PVA solution (the viscosity of the CNT/EPON 828 mixture is about 10^4 orders of magnitude higher than that of the CNT-PSS/PVA solution), which is why greater alignment is observed in the film.

Due to the limitation of our field strength, we have attempted to raise the magnetic susceptibility of the CNTs by using Nickel-coated MWCNT (US4434 from US Research Nanomaterials). However, MWCNTs has low G-band intensity due to the constraints between graphene sheets and the band is easily overwhelmed by the nearby polymer peaks. MWCNTs, coated with magnetic nanoparticles (e.g. Ni or Fe_2O_3), have even poorer Raman signal due to the surface defects resulted from covalent attachment. Figure 4.9 shows the Raman spectrum of a Ni-MWCNT (0.14 wt%)-PSS/PVA film,

with G-band and PVA peak labeled. The raw intensity of the G-band is very low and largely overlapped by the surrounding PVA peak. For future research, SWCNT in high field magnets or different ways of characterizing Ni-MWCNT needs to be explored.

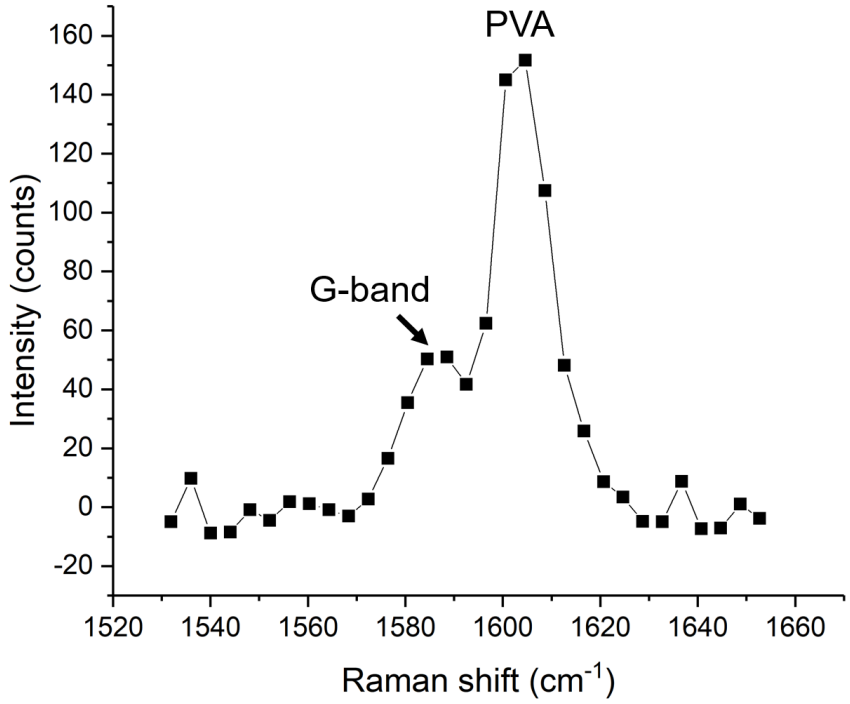

Figure 4.9: Raman spectrum of a Ni-MWCNT (0.14 wt%)-PSS/PVA film.

4.4 Conclusion

Alignment is observed in magnetically-aligned film. Real-time experiments of SWCNTs shows very limited alignment due to the low field strength. Alignment can be improved by increasing the magnetic susceptibility or the magnetic field strength. We have explored the first method by using Nickel-coated MWCNTs However, they do not give satisfactory Raman signal due to the constrained in-plane vibrations and surface defects. Further study needs to be done to investigate the option of increasing field strength such as using the high field magnets at MagLab (Florida,

US), or characterizing MWCNTs with a different technique.

CHAPTER V

Shear Force Alignment

5.1 Introduction

Since most composite molding processes induce a shear force on the composite, investigation of shear alignment could help assess the potential for large-scale production. CNT alignment induced by shear methods can include: 1) mechanical stretching of the cured composite, 2) extrusion and drawing, 3) shear flow, etc. Cured CNT/polymer specimen with CNTs randomly oriented could achieve CNT alignment by the applica- tion of unidirectional tensile strain. CNTs are elongated and aligned in the direction of the tensile strain [28, 29, 31]. Figure 1 shows the distribution of CNTs before (a) and after (b) the application of a 40% tensile strain [31]. Drawing is applied to the uncured CNT/polymer solution and CNTs are aligned when they are extruded [13, 31, 30]. Shear flow induces CNT alignment through the shear force generated by the flow [32–35].

In a polymer solution, the tendency for a rod-like particle to rotate its longitudinal axis into the direction of the shear force, is characterized by the Péclet number, which is the ratio of two competing forces, shear rate and the rotary diffusivity:

$$Pe \equiv \frac{Shear\ Rate}{Rotary\ Diffusivity} = \frac{\gamma}{D_r} \tag{5.1}$$

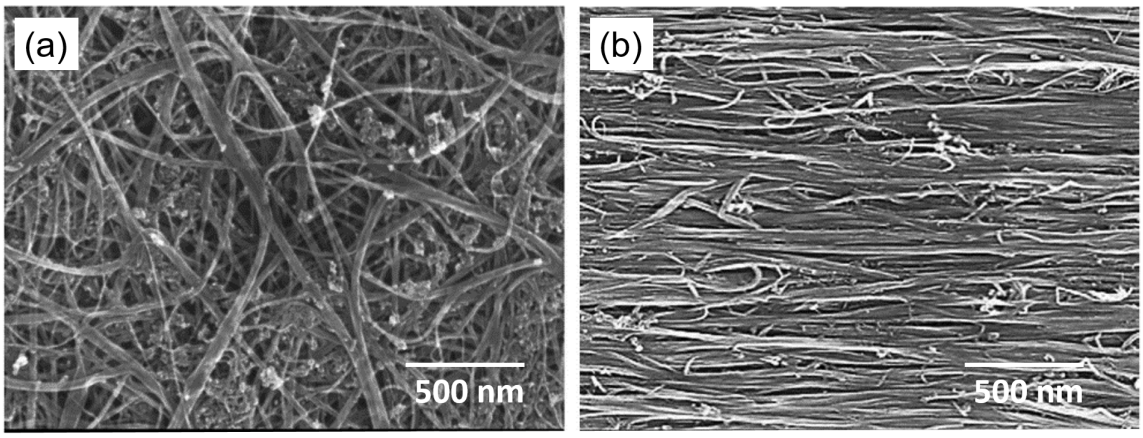

Figure 5.1: SEM images of resin-treated MWCNT networks at strains of 0% (a) and 40% (b) [31]. The strain directions in both images is lateral.

The rotary diffusivity for a fiber in a fluid [57] is:

$$D_r = \frac{3k_BT(\ln L/d - 0.8)}{\eta\pi L^3} \tag{5.2}$$

Where k_B is Boltzmann constant (unit: J/K), T is temperature (unit: K), L and d are CNT's length (unit: m) and diameter (unit: m), and η is viscosity ($Pa \cdot s$). Therefore, if we plug in the expression of the rotary diffusivity:

$$Pe = \frac{\gamma}{D_r} = \gamma\frac{\eta\pi L^3}{3k_BT(\ln L/d - 0.8)} \propto \frac{\gamma\eta}{T} \tag{5.3}$$

The Péclet number, and thus the degree of alignment, is proportional to shear rate and viscosity and inversely to temperature. In the literature, the shear rate effect has been verified by discrete measurements in CNT aqueous solution [58]. Allen et al. has found CNTs lost some of the alignment gained from the shearing due to the high temperature applied during the preparation of CNT composites [59].

We have derived the driving force for an individual CNT aligned by shear force (Appendix E). Our model comes to the same relationships, i.e. the ratio of shear energy and thermal energy is proportional to shear rate and inversely to viscosity and

temperature:

$$\frac{E}{k_B T} \propto \frac{\gamma \eta}{T} \tag{5.4}$$

One common shear flow setup is the torsional flow. The Cambridge Shear Cell (CSS) was a product from the University of Cambridge. It is now fabricated by Linkam Scientific Instruments (Surrey, UK). Details are described in the following experimental section. Researchers have been using this shearing stage to study various CNT behaviors under shear forces. Ma et al. captured the development of a helical banding microstructure from initially randomly oriented clusters of CNT aggregates [60]. Casey et al. studied the shear alignment (discrete measurement) of aqueous CNT solution for CNTs of various chiralities and lengths, with alignment characterized by photoluminescence anisotropy [58]. In this study, we used the Linkam shearing stage to apply shear flow to CNT/EPON 828 mixture and study the kinetics of shear-induced alignment. The findings can potentially be applied to aid next generation CNT composite fabrication.

5.2 Experimental

Shear Flow Setup The Linkam shearing stage (CSS450) generates a shear force between two parallel quartz disks by rotating one of them while keeping the other stationary. As depicted in Figure 5.2, 2 mL of CNT/EPON 828 mixture is confined between the disks with a gap (adjustable) of 1000 μm, at the desired temperature. The sample temperature is maintained through two silver heating elements located either on the top or at the bottom of the two quartz disks and a liquid nitrogen pump for cooling. The laser light penetrates through the sample via a small observation window. The aperture has a diameter of 2.8 mm and a radius of 7.5 mm (center of the observation window to the center of the quartz plate). It is worth noting the

"shear rate" in this thesis refers to the input into the composite system (set on the shearing stage). Due to the linear shear profile, the actual shear rate at the depth of the laser focus is 60% of the input rate. We follow the convention of reporting the input shear rate to compare with other studies in the literature.

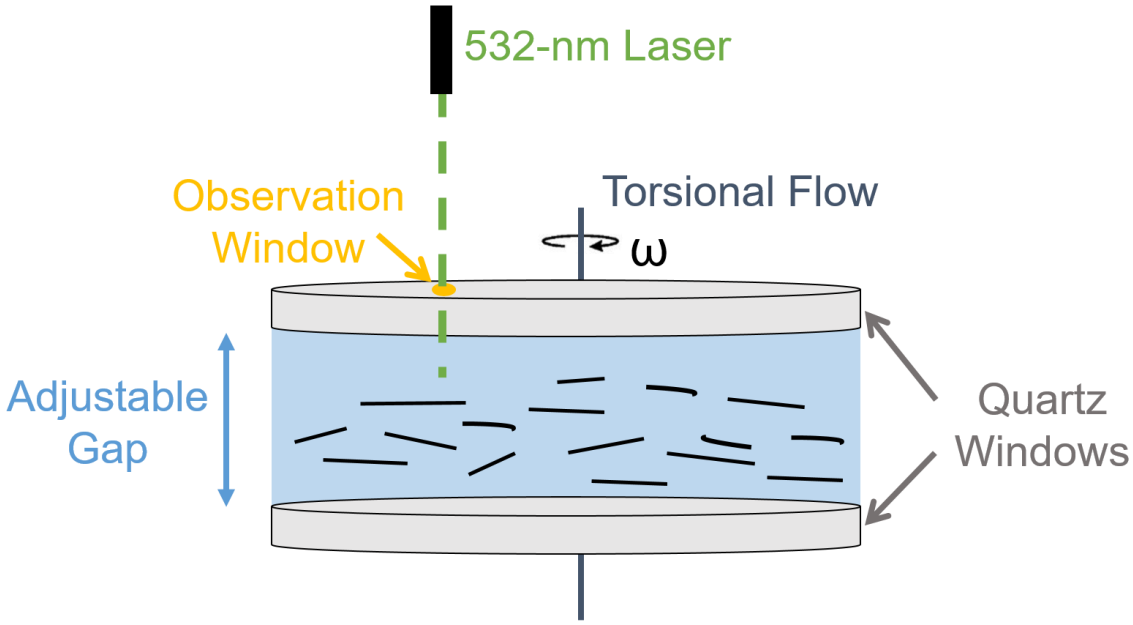

Figure 5.2: Torsional shear flow generated by the Linkam shearing stage.

5.3 Results and Discussion

5.3.1 Shear Force Alignment

We did not prepare any shear-aligned films due to the limitation of our setup. However, real-time experiments measured at different polarization angles (Figure 5.3) clearly show obvious alignment: slight variation in the normalized G-band intensities before shearing; after shearing, maximum intensity occurs in the shear force direction (0^o (H)) and minimum at the perpendicular direction (90^o (V)). This confirms CNTs are oriented preferably along the direction of the shear force.

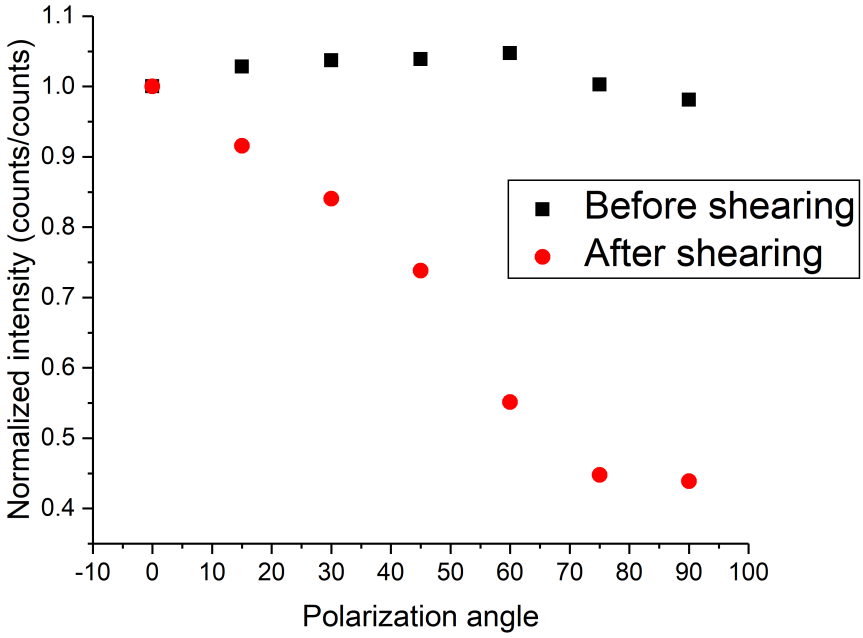

Figure 5.3: Slight variation in the normalized G-band intensities (normalized to the intensity at polarization 0^o) before shearing. After shearing at a rate of 0.1 s^{-1} for 5 minutes, maximum intensity occurs in the shear force direction (0^o (H)) and minimum at the perpendicular direction (90^o (V)).

In real-time experiment, similarly to what we have observed in electric field experiment, the G-band intensity increases as soon as the shear force is applied and gradually reaches a steady-state plateau (in a few minutes), depending on the magnitude of the shear force (Figure 5.4). Higher shear rate leads to faster alignment and a higher plateau value. The higher G-band plateau, or higher degree of alignment, comes from the transition of shorter CNTs, from randomly oriented to preferentially oriented by the shear force. This can be explained by higher Péclet number from Equation 5.3 and has also been observed in electric field experiment (Figure 3.6). The noisier data at higher shear rates is attributed to greater fluctuations observed for the epoxy peak. The increased fluctuations of the epoxy peak at higher shear rates was also observed in neat epoxy samples (Appendix B).

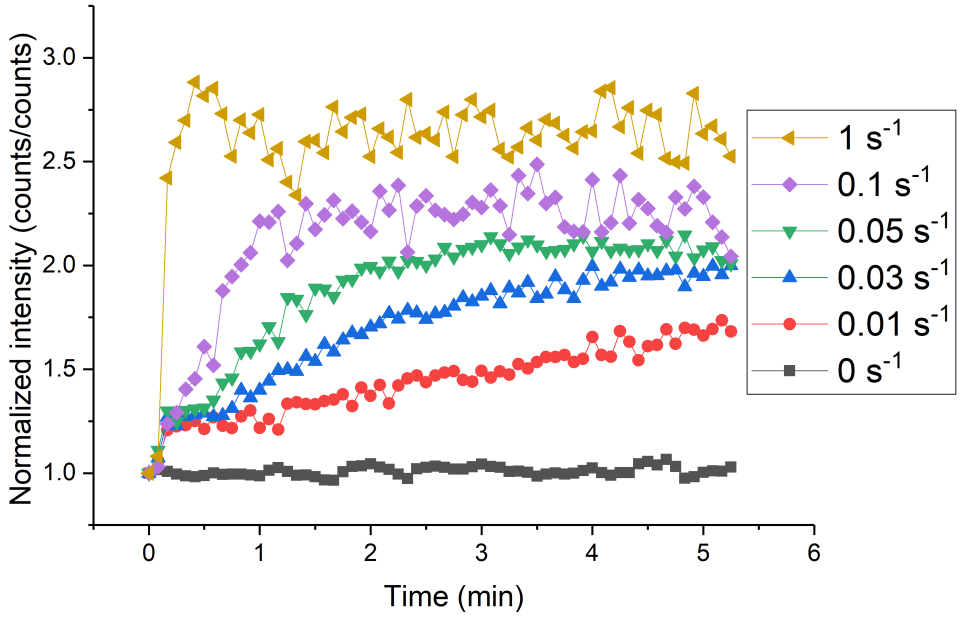

Figure 5.4: Real-time changes of the G-band intensities (at HH polarization) for various shear rates.

Figure 5.5 shows the degree of alignment (in G-band intensity) plotted against the amount of strain. The degree of alignment appears to be linearly proportional to

the strain for low strain. In the high strain (relative) regime, the degree of alignment is, again, determined by shear rate, not the strain, confirming that it is determined by shear rate overcoming thermal randomization.

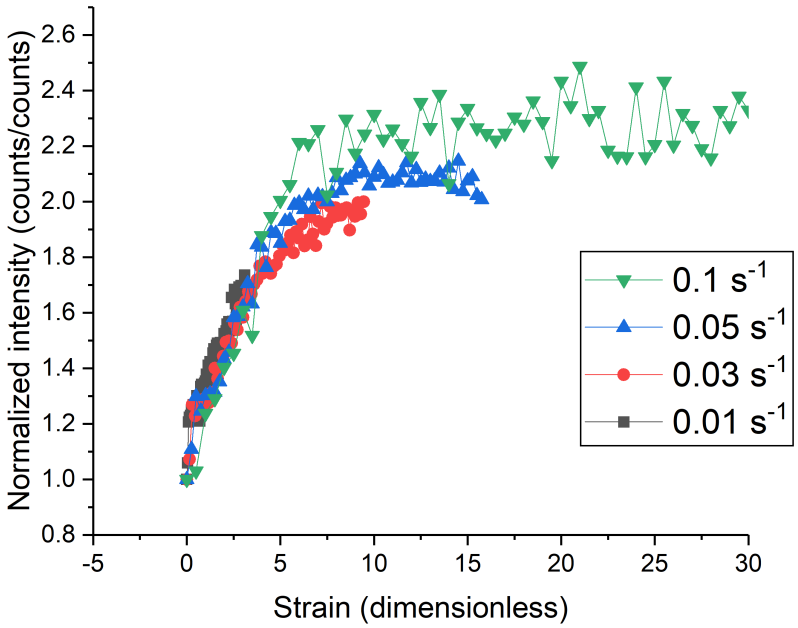

Figure 5.5: G-band intensity as a function of the input strain for selected shear rates.

Real-time alignment experiments were conducted at different temperatures and an example (aligned at a shear rate of 0.1 s^{-1}) is shown in Figure 5.6. At higher temperature, the G-band intensity reaches a lower asymptote. However, the rate of change of intensity appears to be independent of temperature. This is because the degree of alignment is controlled by thermal randomization (as reflected in the Péclet number) while the speed of alignment is only controlled by the rotary speed of the quartz plate.

The alignment is found to be reversible and reproducible. In Figure 5.7, a CNT/EPON 828 mixture is aligned at a shear rate of 0.1 s^{-1} and at room temperature of 21 ^{o}C) for 10 minutes to reach the steady-state plateau. Then the shear rate is increased to 1 s^{-1} (t = 13 min) and then decreased back to 0.1 s^{-1} (t = 18 min).

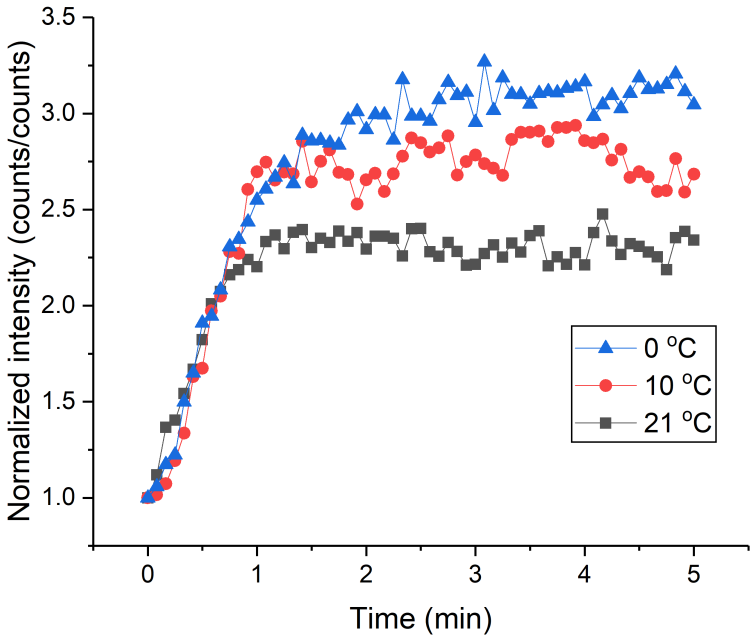

Figure 5.6: Real-time changes of G-band intensities for CNT/EPON 828 suspensions aligned under a shear rate of 0.1 s^{-1} at temperatures of 0, 10 and 21 ^{o}C.

The G-band intensity increases (almost) instantaneously and reaches a new higher plateau when the shear rate is first raised to 1 s^{-1}. It decreases to the original plateau when the shear rate is lowered back to 0.1 s^{-1}. In a similar manner, when an aligned CNT/EPON 828 suspension under a constant shear rate is subjected to a change in temperature, the G-band intensity changes accordingly in response to the temperature change. Figure 5.8 shows how the plateau intensity (aligned at a shear rate of 0.1 s^{-1}) increases and decreases back and forth under a temperature cycling between 21 and 0 ^{o}C. The temperature is changed at a rate of 20 ^{o}C/min for both cooling and heating. From Figure 5.7 and 5.8, we conclude that the G-band intensity is reversible and reproducible: the plateau intensity is only determined by the experimental conditions, i.e. shear rate and temperature, and does not depend on the history of the sample.

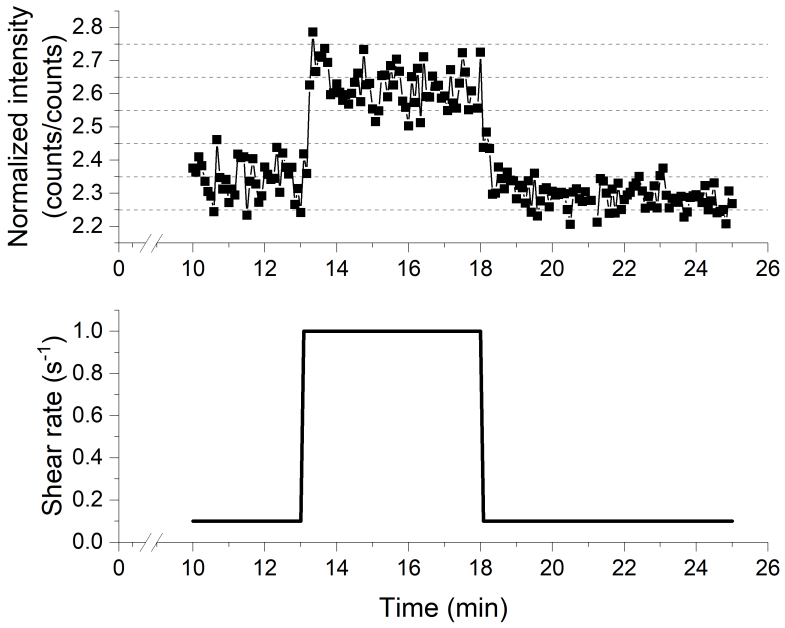

Figure 5.7: G-band intensities (top) changes with the change of the shear rate (bottom). The CNT/EPON 828 mixture is aligned at a shear rate of 0.1 s^{-1} (21 ^{o}C) for 10 minutes and then subjected to changes between 0.1 and 1 s^{-1}.

5.3.2 High Shear Rate

As shown in Figure 5.4, increasing shear rate raises the steady-state plateau of the G-band curve. However, when the shear rate is very high, the G-band intensity starts to decrease after an initial increase from alignment (Figure 5.9). This might be because the suspension flows fast under a high shear rate, making it easier for CNTs to meet and form large bundles or aggregates. These bundles or aggregates give poor Raman signal due to restricted in-plane vibrations. Allen et al. has visually observed precipitation of CNT aggregates in an aqueous CNT solution due to high shear in the Linkam shearing stage [61]. Further study needs to investigate if our hypothesis is valid and how to prevent shear-induced CNT bundling and aggregation.

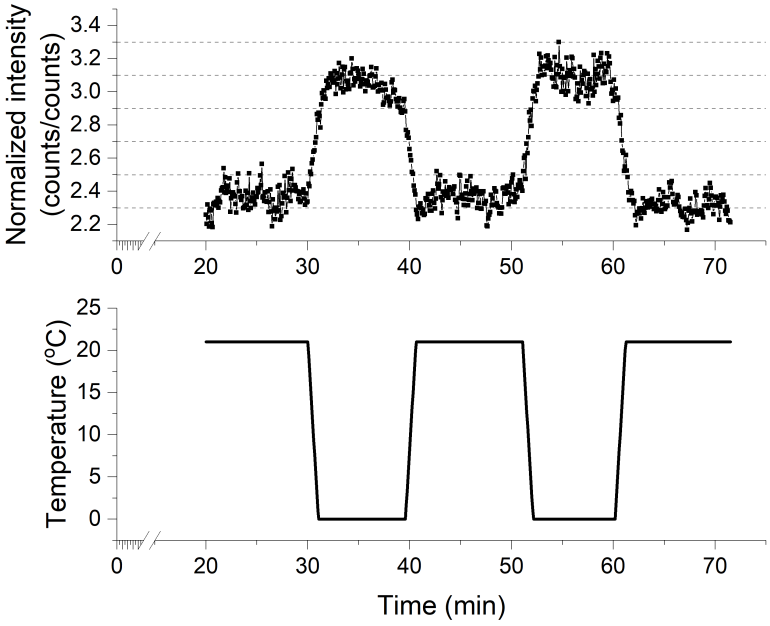

Figure 5.8: G-band intensities (top) changes with the change of the temperature (bottom). The CNT/EPON 828 mixture is aligned at a temperature of 21 ^{o}C (0.1 s^{-1}) for 20 minutes and then subjected to changes between 21 and 0 ^{o}C. The temperature is changed at a rate of 20 ^{o}C/min for both cooling and heating.

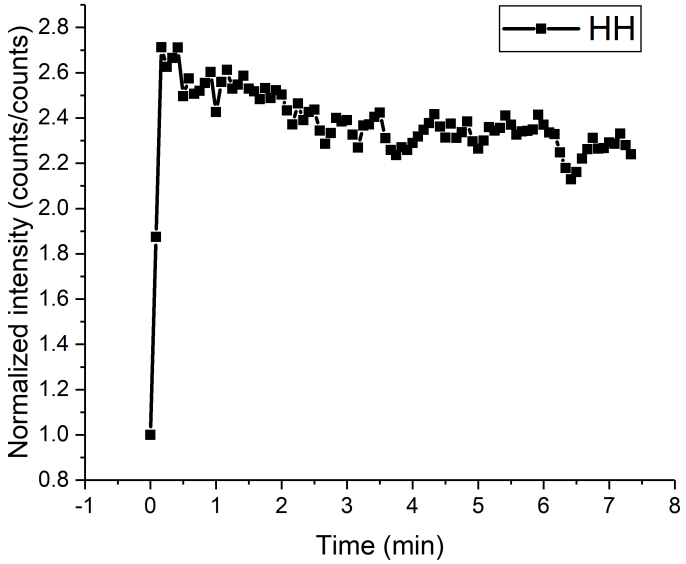

Figure 5.9: G-band intensity decreases after an initial increase when subjected to a high shear rate of 10 s^{-1} (21 ^{o}C).

5.3.3 Low and High Temperature

Despite the temperature effect seen in Figure 5.6, no obvious alignment is observed when temperature is decreased to -20 ^{o}C (Figure 5.10), even for shear rates as high as 10 s^{-1}. The epoxy matrix becomes extremely viscous when cooled to near the glass transition temperature (T_g), of around -20 to -15 ^{o}C. Therefore the CNT/EPON 828 mixture is almost transformed into solid and shear flow can no longer be induced.

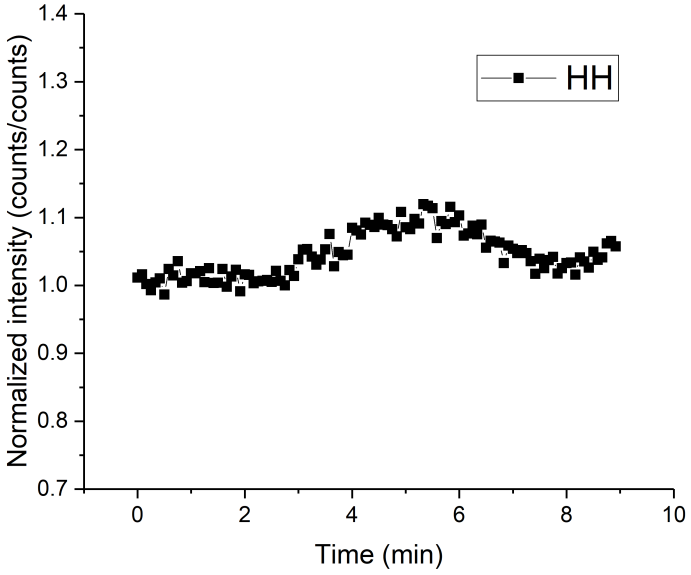

Figure 5.10: No obvious alignment is observed at the low temperature of -20 ^{o}C (0.1 s^{-1}).

On the other hand, when the temperature gets too high, the G-band intensity at VV polarization unusually increases (Figure 5.11(a)). However, it does not mean a portion of CNTs is aligned at the VV direction. In Figure 5.11(b), the plateau intensity increases at all polarization angles. The H/V ratio is 1.1, which indicates there is no alignment in the mixture. This is reasonable because the viscosity of the epoxy decreases significantly at high temperature and together with the high thermal energy, the randomization energy far exceeds the alignment energy. In other words, Péclet number is very small. The intensity increase at all polarization angles appears

to be a measurement artifact and it is unclear why it occurs at high temperature. Attention should be paid in the future to uncover this issue.

5.3.4 Shear Force vs. Electric field

The alignment behavior under shear force is compared with its electric field counterpart. In the effect of field strength, similar alignment curves are observed in both cases: the alignment rises quickly at the beginning with a decreasing speed until it reaches a steady-state plateau (Figure 5.4 and 5.12). In both cases, high field strength leads to higher degree of alignment as well as a faster speed. In addition, alignment occurs faster under shear force than in electric field. At a shear rate of 1 s^{-1}, the signal reaches the plateau in less than 30 seconds in a viscous epoxy (Figure 5.4), compared to an AC field of 1100 V/cm reaching the plateau in around 5 minutes (Figure 5.12).

The temperature study for electric field experiment is shown in Figure 5.13 [49]. High temperature, different to our observation in shear force experiment, does not affect the final degree of alignment, but does enable faster alignment. Unlike shear rate determining alignment speed in the shear force experiment, the speed of alignment is controlled by the friction force from the polymer matrix. When temperature increases, the viscosity of the epoxy matrix decreases, thus lowering the friction force and making it easier to alignment. The degree of alignment, however, is not found to be affected by temperature. It is unclear at this point if it is due to the specific range of the temperatures tested or the electric model is incomplete. The alignment behavior in electric field at a broader range of temperatures needs to be further studied.

Another difference is the electric field alignment appears to have a minimum field strength (Figure 5.12), below which no obvious alignment is observed. However, the G-band intensity is found to be increasing at the minimum shear rate of 0.003 s^{-1} (machine limit) in Figure 5.14. In the future, a polymer system with lower viscosity

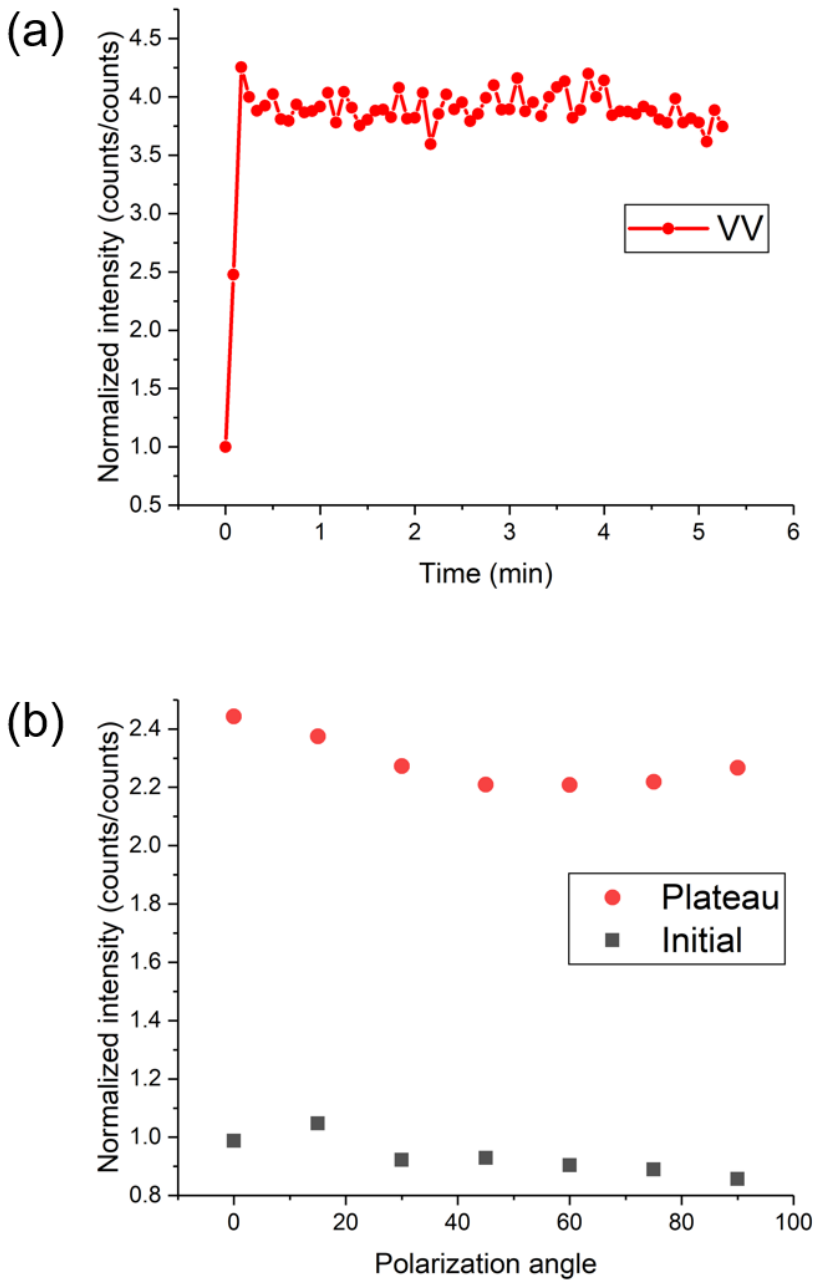

Figure 5.11: G-band intensity at VV polarization increases at the high temperature of 90 ^{o}C (a). Initial and plateau intensity at different polarization angles (b). $0^o/90^o$ corresponds to H/V polarization. The H/V ratio is 1.1. Shear rate is 0.1 s^{-1} for both cases.

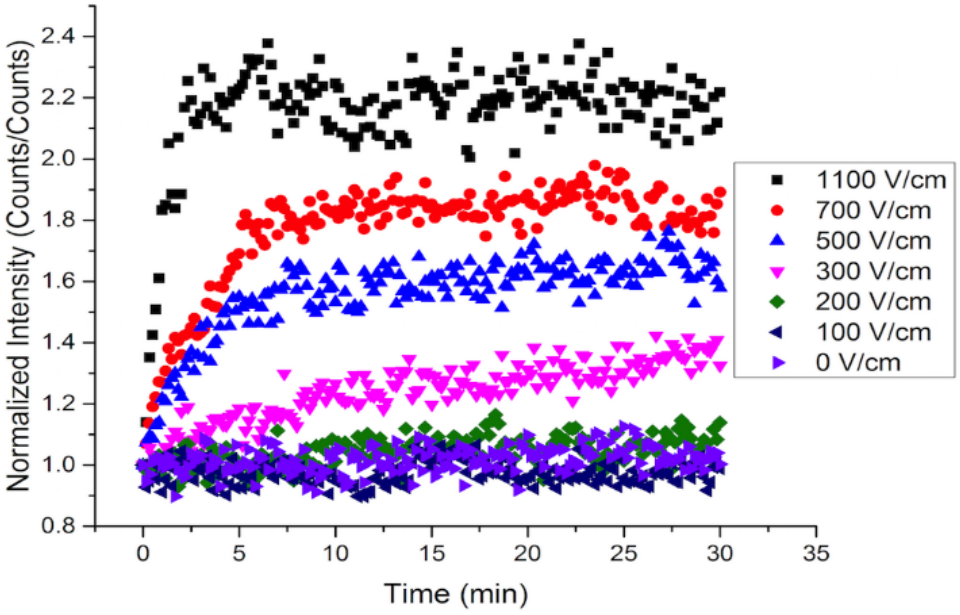

Figure 5.12: G-band intensities a function of time for selected electric field strengths at 1 kHz and a 0.005 wt% CNT concentration, at room temperature [49].

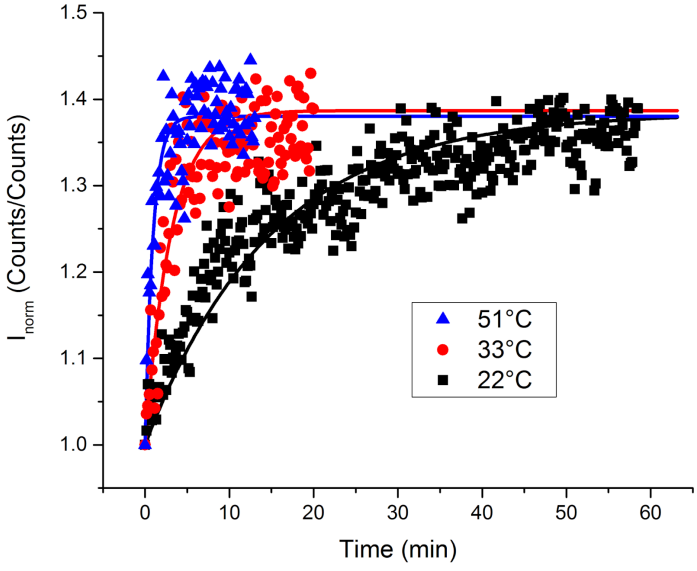

Figure 5.13: G-band curves at selected temperatures for an electric field strength of 300 V/cm at 1 kHz and a 0.005 wt% CNT concentration [49].

is needed to investigate the occurrence of a minimum field strength.

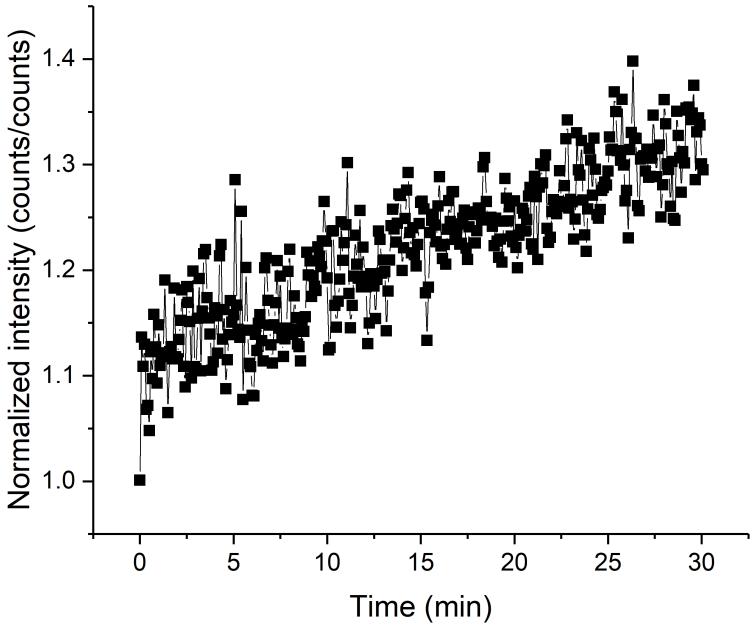

Figure 5.14: G-band intensity increases at the minimum shear rate of 0.003 s^{-1} (machine limit).

The release of alignment (stopping the field after the steady-state plateau) takes longer than the time to reach the plateau, in both shear force and electric field. Figure 5.15 shows the release curves of shear-aligned (0.1 s^{-1}) and electrically-aligned (1100 V/cm) CNTs in CNT/EPON 828 mixture. The G-band intensity, in both cases, roughly decreases to the original state, suggesting CNTs has returned to the state of random orientation. The randomization occurs immediately when the field is turned off, indicating the applied field needs to be maintained during the course of alignment, in order to capture the full potential of alignment when fabricating aligned CNT composites.

The release curve for shear force alignment appears to have larger fluctuations that electric field alignment. Possible reason might be due to residual flow and nonuniform dispersion of CNTs. During shearing, the composite mixture flows at a high speed and

the Raman signal collected from the observation window is an average of intensities from a series of continuous locations. Further study needs to be done to determine the post-alignment dynamics in the CNT/EPON 828 mixture.

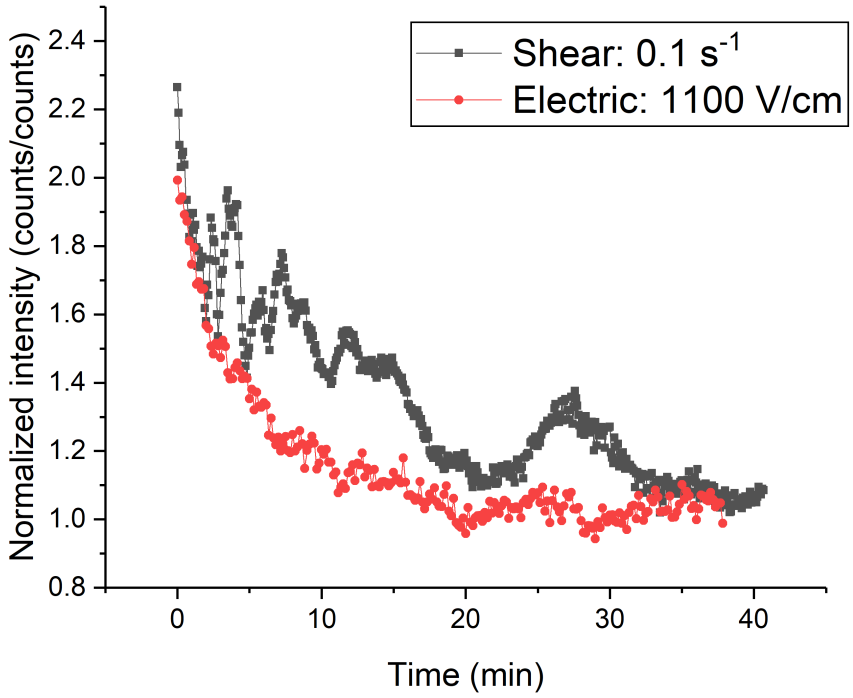

Figure 5.15: Release curves of shear-aligned (0.1 s^{-1}) and electrically-aligned (1100 V/cm) CNTs in CNT/EPON 828 mixture. Electric field data is from Dr. Wesley Chapkin.

It is worthwhile compare the degree of alignment achieved in these two cases. Figure 5.16 shows the degree of alignment (in HH/VV ratio) for selected shear rates (0.01, 0.03, 0.1 and 1 s^{-1}) and a range of temperatures (-10, 0, 10, 21 ^{o}C). The HH/VV ratio generally increases with increasing shear rate and lowering temperature (with some exceptions). The ratio is significantly higher when temperature decreases to -10 ^{o}C, due to substantially increased viscosity (higher Péclet number).

The maximum degree of alignment in the figure is 9.7, which falls at the higher end of electric field experiment in Table 5.1. But electric field alignment would require

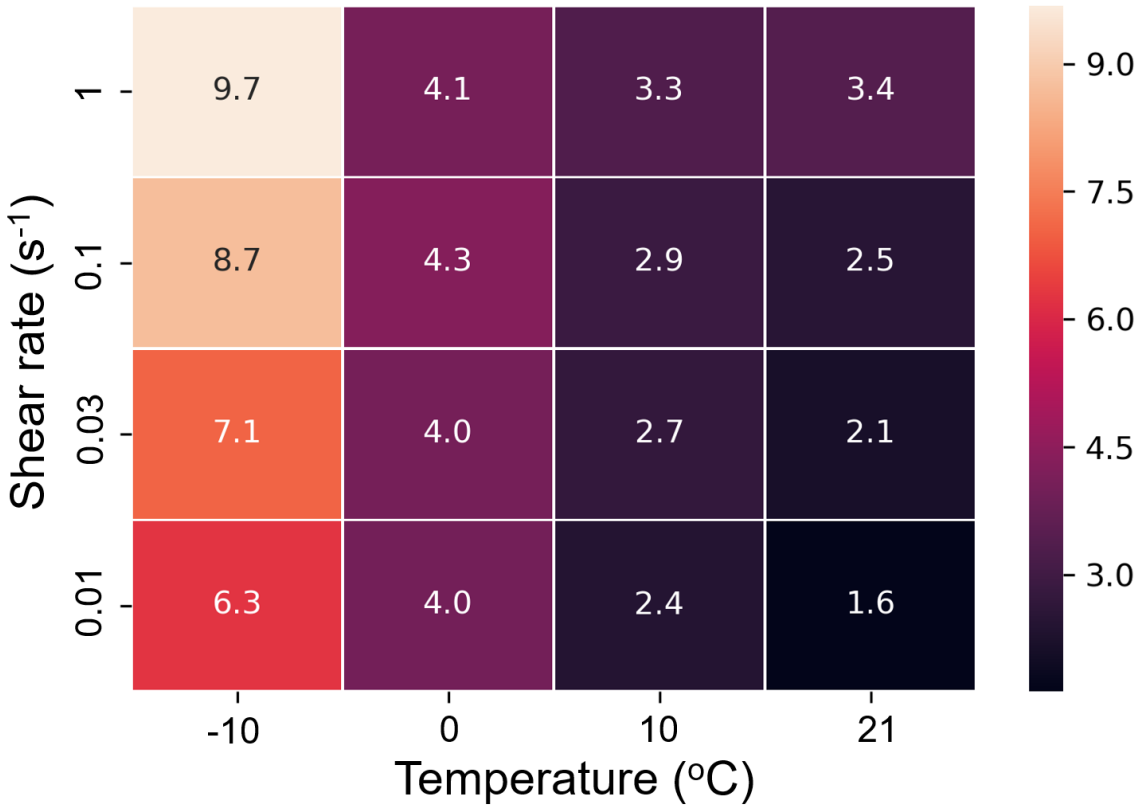

Figure 5.16: HH/VV ratios for selected shear rates (0.01, 0.03, 0.1 and 1 s^{-1}) and a range of temperatures (-10, 0, 10, 21 ^{o}C).

a very high field strength of a few thousand V/cm that is difficult to set up and may cause safety issues. High electric field strength would also cause Joule heating that could potentially interfere with the alignment. On the other hand, a shear rate of 1 s^{-1} is moderate and can be easily achieved. Other forms of shear force, such as mechanical stretching or extrusion, are found to induce higher HH/VV ratios. These are typically applied during processing (extrusion) or post processing (stretching). It is promising to combine multiple alignment methods to further improve the degree of the alignment.

Table 5.1: A survey of maximum HH/VV ratios for alignment under electric field and shear force. Some data are from references in [49]. Notice for [58], the ratio is measured in photoluminescence (PL) instead of Raman.

Alignment Method	**Maximum Field Strength**	**Alignment Time**	**Polymer Matrix**	**Maximum HH/VV**	**Ref.**
Electric	330 V/cm, 1 kHz	120 min	EPON 828 (cured)	2	[49]
Electric	435 V/cm, 10 kHz	10 min	UDMA/ HDDA blend	2.5	[20]
Electric	3000 V/cm, 1 kHz	30 min	UDMA/ HDDA blend	7.1	[62]
Electric	5000 V/cm, 1 kHz	30 sec	EPON 828 (uncured)	7.9	[49]
Torsional flow	330 s^{-1}		SDBS (aqueous)	4 (PL)	[58]
Torsional flow	1 s^{-1}, -10 ^{o}C	15 min	EPON 828 (uncured)	9.7	This study
Mechanical Stretching			Polyacrylic acid	12	[63]
Extruded fibers			PMMA	20	[64]

5.4 Conclusion

Real-time CNT alignment is successfully measured under a shear flow. The effects of shear rate and temperature have been investigated and are found to match the

expression of the Péclet number as well as our model of driving force for alignment. The degree of alignment is determined by thermal randomization and the alignment speed is controlled by shearing. Alignment behavior becomes complicated when shear rate is high and when temperature is either too low or too high. A comparison between alignment by shear force and the electric field demonstrates similar kinetics and different driving forces. The degree of alignment is benchmarked and found to be high among the studies in the literature.

CHAPTER VI

Conclusion

6.1 Summary

CNT alignment is crucial in determining the mechanical properties of CNT composites. Prior work only focused on discrete measurements, leaving a theory of alignment kinetics lacking. We developed an in *in situ* Raman spectroscopy technique that enables monitoring CNT alignment in polymer matrix in real time. This technique is applied to study alignment behavior under electric field, magnetic field and shear force.

Chapter II presents the experimental details of our Raman characterization method. The real-time CNT alignment changes is monitored by tracking the G-band intensity from the polarized Raman spectra of CNT. Processing and analysis of the spectra are described.

In Chapter III, this technique is first used to study the real-time alignment in an AC field. The G-band intensity in the alignment direction increases over time, confirming CNTs gradually aligning in the direction of the electric field. Higher field strength leads to faster alignment and a higher steady-state plateau.

Chapter IV explores the alignment behavior under a magnetic field. Though alignment is observed by discrete measurement on CNT-PSS/PVA film, the real-time data shows smaller and more scattered changes (of G-band intensity), compared to the

observations in electric field. A literature survey and the *Minimum Volume Theory* suggest smaller changes come from the small magnetic susceptibility of our pristine SWCNTs. The data scattering comes from translational motion of CNTs, which is observed in CNT agglomerations. Future research needs to consider CNTs with high magnetic susceptibility or using other characterization method.

Chapter V concentrates on shear-induced alignment. The Raman technique is successfully applied to monitoring alignment in a shear flow and achieves similar alignment behavior as in electric field. Higher field strength results in faster alignment as well as a higher plateau. Higher temperature, on the other hand, lowers the degree of alignment but does not affect the alignment speed. These effects of field strength and temperature match the expression of the Péclet number and our model of driving force of alignment for an individual CNT in a shear flow. The alignment behavior gets complicated at certain shear rates and temperatures. When the shear rate is as high as 10 s^{-1}, the G-band intensity decreases after an initial increases. CNT bundling and aggregation are suspected to occur, resulting in poorer Raman signal. No obvious alignment is observed when temperature decreases to -20 ^{o}C. When temperature is too high (e.g. 90 ^{o}C), a measurement artifact that intensity increases in all polarizations occurs and the reason is unclear. A comparison between shear alignment and electric field alignment shows they share similar field strength effects and different temperature effects. This suggests different driving forces: shear alignment is strain-controlled while electric field alignment is force controlled. The release curve appears similar but shear alignment has more fluctuations in the G-band signal, which might be due to the residual flow and nonuniform dispersion of CNTs. The randomization occurs immediately after the applied field is off and takes longer (than alignment) to reach the original level of intensity. This implies the importance of continuously applying the force during the fabrication process of aligned composite samples, in order to capture the full potential of alignment. The degree of shear-induced

alignment is comparable to its electric field counterpart. However, the electric field strength needed is extremely high.

6.2 Future Work

This thesis investigates the kinetics of CNT alignment in the polymer matrix. An *in situ* technique is developed to monitor CNT alignment in real time using Raman spectroscopy. In the future, this technique can be used to further study the existing work in depth and to create standard protocols for fabrication process in composite manufacturing. The technique is so far, to our best knowledge, the most accurate and convenient method for real-time CNT alignment measurement. It can be adapted to study almost all existing *ex situ* alignment methods.

Chapter II describes the Raman spectroscopy used in this study. A 785-nm green light laser was the excitation source. Most recent research suggests lasers of different wavelengths may excite different populations of CNTs, e.g. CNTs of various chiralities [58]. A different laser, e.g. red light laser with wavelength over 1000 nm, can be used to perform the same experiments in this work and to compare the results.

The electric field alignment in Chapter III has been further studied by my colleague, Dr. Wesley Chapkin. Findings as well as future work can be found in [49].

Chapter IV discusses the issues of our magnetic field alignment: low magnetic susceptibility of our pristine CNTs. To increase the signal-to-noise ratio of in Raman spectra, we can apply to use the high field magnet at the MagLab in Florida, or find another characterization method that works for CNTs coated/infiltrated with magnetic nanoparticles. Such a method might still be a spectroscopic technique because it is easier to set up real-time measurement, as described in Chapter II. The data scattering resulted from CNT translation could be reduced by using an AC magnet because the alternating field is expected to lock CNT in place.

The findings of shear alignment in Chapter V is of great importance for composite

manufacturing. Many processes involve applying shear force on the uncured composite during the fabrication. Examples include extrusion and drawing. It has been found alignment is indeed achieved from these processes [13, 31, 30]. The studied kinetics can help achieve full potential of alignment. For instance, the influence of temperature would help predict the degree of alignment in the cured composite sample and motivate the choice of polymer matrices with low curing temperatures. The equation of Péclet number (Equation 5.3) suggests alignment has a large dependency on the length distribution of the tubes. This length effect has been corresponding to the alignment curve in electric field alignment [49] and needs to be verified for the shear case. Moreover, the release curve (Figure 5.15) can be associated with the length distribution as well. Since it is easy to apply high field strength in shear force than in an electromagnetic field, low-viscosity systems (aqueous CNT solutions, e.g. CNT-PSS/PVA solution used in this work), can be studied in the future. Real-time characterization has not been achieved for these systems in an electromagnetic field due to large randomization energy. The unusual alignment behaviors, i.e. under high shear rate and at low/high temperature, needs to be investigated.

Finally, this work only studied the EPON 828 matrix and future work can be extended to other common industrial polymers, e.g. polyethylene (PE) and Polymethyl methacrylate (PMMA), etc. Our Raman technique is an indirect characterization method that sees a collection of CNTs. To visually observe CNT alignment for small-size CNTs, particularly individual SWCNTs, we might need to use *in situ* TEM with special sample-holders where an external field can be applied.

APPENDICES

APPENDIX A

Cost Analysis of Adding CNTs to Polymer Composites

Figure 1.2 shows CNT prices are expected to drop significantly with the increasing production volume. Zhang et al. predicted the cost of CNTs will drop to \$10-30/kg in the future [10]. Carbon fiber currently costs about \$20/kg (PAN precursor) and is predicted to be lowered to \$10/kg [65]. Epoxy costs about \$2.5/kg [66] and we assume price does not change in the future. Table A.1 shows the current and forecasted costs of epoxy, CNTs and carbon fiber. In the following calculations, the lower bound of the current MWCNT cost (\$100/kg) is taken as the current cost of CNTs and the higher bound of the forecasted CNT cost (\$30/kg) is taken as the CNT cost in the future. Bolded numbers in Table A.1 are used for the following calculations.

Table A.1: Current and forecasted costs of epoxy, CNTs and CF.

Material Cost (\$/kg)	**Current**	**Forecast**
Epoxy	**2.5**	**2.5**
Carbon nanotube	50k-400k (SWCNT) **100**-25k (MWCNT)	10-**30** (SWCNT or MWCNT)
Carbon fiber	**20** (PAN-based)	**10**

Bai et al. found that the addition of 0.5 wt% MWCNTs into epoxy matrix resulted in 77% increase of composite tensile modulus and 32% increase of composite tensile

strength [67]. Davis et al. incorporated 0.5 wt% functionalized CNTs into carbon fiber reinforced epoxy composite laminates and obtained 24% and 18% increase in tensile modulus and tensile strength respectively, compared with neat carbon fiber epoxy composite laminates [68]. The laminates have a 55% fiber volume content [60] or 64% in weight [69].

The enhancement in mechanical properties in the above two findings can be normalized with respect to the cost increase due to the addition of CNTs. Here we take Bais results as an example to calculate, in the future, what percentage of improvement in mechanical properties we will get if we pay one percent increase in material cost. First we consider the mechanical properties of the neat epoxy to be 100% and relatively the enhanced tensile modulus and strength are 177% and 132%. The current and forecasted costs of the CNT/epoxy composite are estimated, with material costs given in Table A.1. The relative cost increases due to the addition of CNTs are calculated by first taking the difference between the forecasted costs of the composite and the neat epoxy, then divided by the forecasted cost of the neat epoxy.

The addition of 0.5 wt% CNT into the epoxy raises the cost from \$2.50/kg to \$2.64/kg, a 5.50% $((2.64 - 2.50)/2.50)$ increase in cost. Finally the relative enhanced tensile modulus and strength are divided by this cost increase ratio, giving 14.0 (77%/5.50%) and 5.82 (32%/5.50%) respectively. This means if we invest one more percent in material cost, we will achieve 14.0% and 5.82% increase in tensile modulus and strength. The same analysis procedure is applied on CNT/CF/epoxy composite. Table A.2 summarizes the costs of CNT composites and the normalized enhancement in mechanical properties over cost for CNT/epoxy composite and CNT/CF/epoxy composite. Table A.2 illustrates that the incorporation of CNTs into neat materials is becoming more cost-effective, e.g. using forecasted costs, a 1% cost increase in CF/epoxy composite enables over 10% increase in both tensile modulus and tensile strength. The results described above might be improved even further with improved

dispersion and alignment techniques.

Table A.2: Materials cost and normalized enhancement in tensile modulus and strength for 0.5 wt% CNT/epoxy and 0.5 wt% CNT/CF/epoxy composite.

	CNT/epoxy		**CNT/CF/epoxy**	
	Current	**Forecast**	**Current**	**Forecast**
Cost ($/kg)	2.99	2.64	14.1	7.41
Modulus/cost (%/%)	3.95	14	7.62	15.5
Strength/cost (%/%)	1.64	5.82	5.71	11.6

APPENDIX B

Epoxy Peak Fluctuation

The epoxy peak at 824 cm^{-1} is used as an indicator of the fluctuation of the composite system. Because the epoxy chains do not align and are always randomly oriented. Figure B.1 shows the epoxy peak intensity, in pure EPON 828 solution, before and after shearing is applied (at $t = 2\ min$). Similar curves are observed in electric and magnetic field. The small changes indict epoxy chains are not affected by shearing and thus can be used as a measure of the noise of the composite system.

However, when the applied shear rate is high (e.g. 1 s^{-1}), larger and seemingly cyclic fluctuations of intensity is seen (Figure B.2). This causes greater fluctuations for higher shear rates in Figure 5.4 as G-band intensity is normalized according to Equation 2.1.

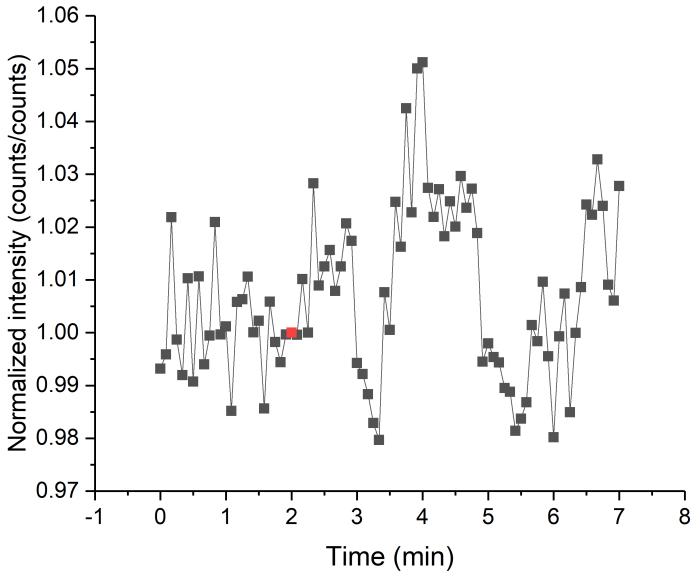

Figure B.1: Epoxy peak intensity (pure EPON 828 solution) barely changes under shearing. A shear rate of 0.01 s^{-1} is applied at time $t = 2$ *min* (red), to which all other data is normalized to.

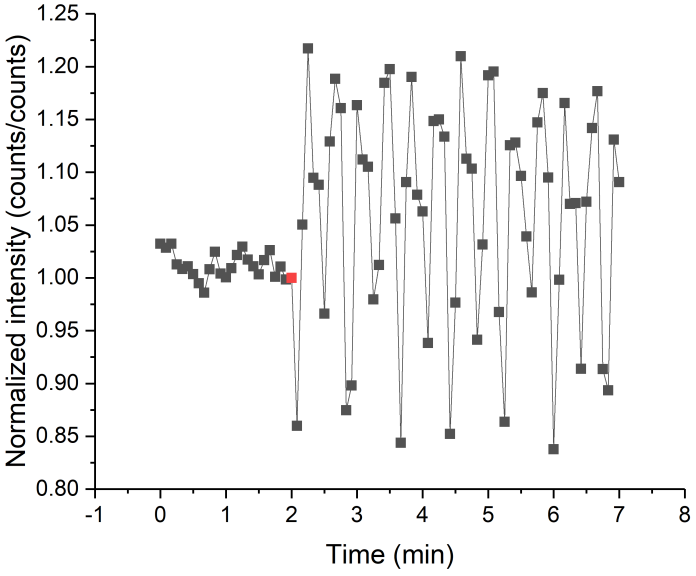

Figure B.2: Epoxy peak intensity (pure EPON 828 solution) starts to fluctuate when a high shear rate (1 s^{-1}) is applied. Shearing is applied at time $t = 2$ *min* (red), to which all other data is normalized to.

APPENDIX C

Nonuniform Alignment in Magnetically-aligned Film

The local variations in materials is observed in magnetically-aligned films. CNT-PSS/PVA films were fabricated in standardized sizes, with a length of 35 mm and width of 5 mm. The thickness is around 100 m. The middle region with a length of 25 mm was exposed to magnetic field. Polarized Raman spectroscopy is taken at uniformly distributed spots on the film, with a spacing of 4 mm in length and 1.5 mm in width. Spots along the length are labeled 1 to 7, and a, b, and c along the width. Figure C.1 shows a schematic of the measurement points on the film.

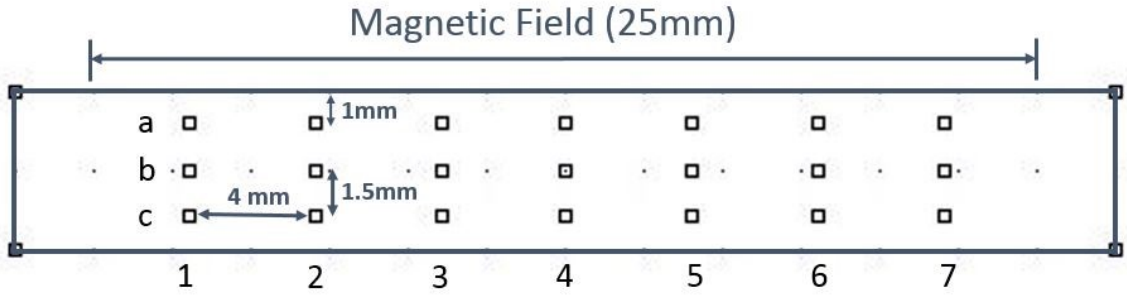

Figure C.1: Schematic of measurement points on a standardized magnetically-aligned CNT-PSS/PVA film.

Table C.1 shows the H/V ratio at different spots for a film aligned in a magnetic field of 0.6 T. The discrepancies in H/V ratios indicate that the magnetic field is not uniform and the degree of alignment is sensitive to locations in the field. The average of H/V ratios (last column) in the b line (middle row) is higher than a line and c line.

Table C.1: H/V ratios for a CNT-PSS/PVA film aligned in a magnetic field of 0.6 T.

H/V	**1**	**2**	**3**	**4**	**5**	**6**	**7**	**Average**
a	0.94	0.98	1.12	1.29	1.22	1.10	1.12	1.11
b	2.31	1.84	1.57	1.62	1.14	1.52	1.87	1.70
c	1.17	1.33	0.85	1.19	0.81	1.03	1.30	1.10

Similar pattern of H/V ratios are found in the film aligned in a lower field of 0.4 T (Table C.2). Moreover, the average of the total 21 H/V ratios in Table C.1 is 1.30 while that for Table C.2 is 1.24, likely implying higher field strength leads to higher degree of alignment.

Table C.2: H/V ratios for a CNT-PSS/PVA film aligned in a magnetic field of 0.4 T.

H/V	**1**	**2**	**3**	**4**	**5**	**6**	**7**	**Average**
a	1.11	1.43	0.83	1.24	1.25	0.92	1.48	1.18
b	1.42	1.53	1.51	1.80	1.42	1.60	1.35	1.52
c	1.24	1.11	0.77	0.86	1.39	0.94	0.75	1.01

APPENDIX D

Minimum Volume of CNT for Magnetic Field Alignment

Kimura proposed the following equation to calculate the minimum volume required for alignment to overcome thermal energy [54]:

$$V > \frac{2\mu_0 k_B T}{|\chi| B^2}$$

Where the V is the minimum volume (m^3), μ_0 is the vacuum permeability (H/m), k_B is the Boltzmann constant (J/K), T is absolute temperature (K), χ is the volumetric susceptibility (dimensionless) and B is the magnetic field (T).

Pristine SWCNTs have volumetric magnetic susceptibility of about 10^{-14} [22, 70] and assume a magnetic field of 1 T, the minimum volume needed is calculated to be 10^{-13} m^3, orders of magnitude larger than the actual volume of our SWCNT, which is 10^{-24} m^3.

On the other hand, MWCNTs decorated (Figure 4.1(a) [25]) or infiltrated (Figure 4.1(b) [26]) with Fe_3O_4 nanoparticles and their corresponding applied field strengths are summarized in Table D.1. The actual volumes of these treated MWCNTs are larger than the calculated minimum volumes.

Table D.1: The decorated and infiltrated MWCNTs have calculated minimum volumes smaller than their actual volumes.

CNT Type	**Field Strength** (T)	**Volumetric Susceptibility**	**Minimum Volume** (m^3)	**Actual Volume** (m^3)
Decorated MWCNT	0.2	0.07	10^{-23}	10^{-20}
Infiltrated MWCNT	0.1	0.89	10^{-24}	10^{-18}

APPENDIX E

A Theoretic Derivation of the Driving Force for Alignment

In order for the alignment to occur, the applied shear energy needs to overcome the thermal energy k_BT. Thus the driving force for alignment can be expressed as the ratio of the shear energy over thermal randomization: E_{shear}/k_BT. This appendix derives the expression for this ratio, from an energetic perspective.

Alignment Force An individual CNT can be treated as a 1D rod-like particle [57]. In Figure E.1, the CNT initially lies in the position which forms an angle of θ_i, with the perpendicular direction of the shear flow. Then, under the shear force, it is aligned closer to the shear force direction, from θ_i to θ_j. In this case, the pivot is chosen at one end of the CNT. However, if the pivot is selected at the center of the CNT, the following derivations should be similar and do not affect our conclusion.

The alignment torque, T_{shear}, comes from the force perpendicular to the tube F_{align}, which is a decomposing part of the force from shear flow F_{flow}:

$$F_{align} = F_{flow} \cos\theta \tag{E.1}$$

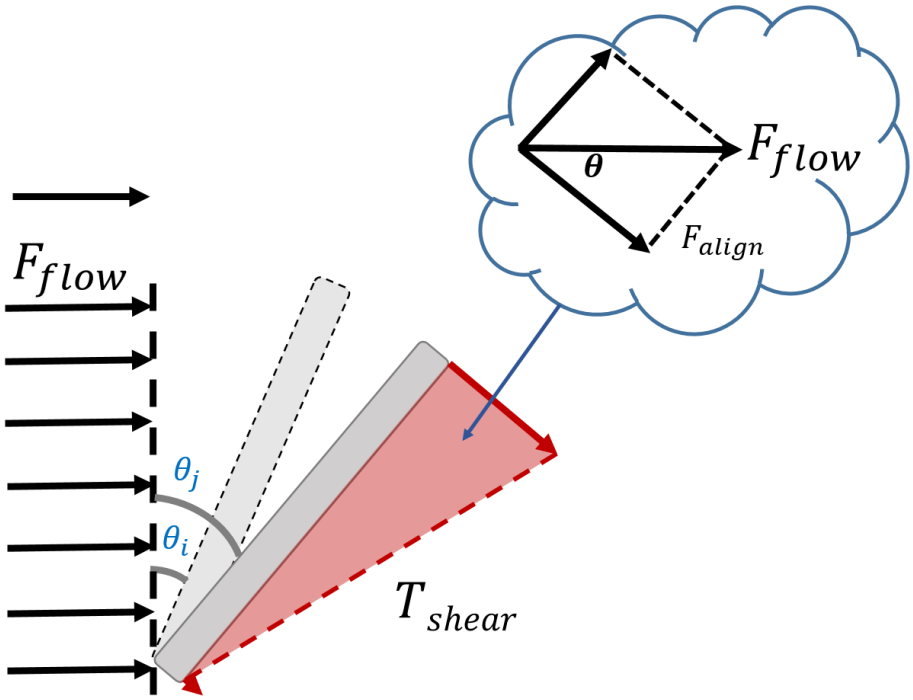

Figure E.1: Shear force acts on a single CNT and creates an alignment torque.

The force from the shear flow F_{flow} is:

$$F_{flow} = \tau_{shear} \cdot A_{cross} = (\gamma\eta)(\pi r L) = \gamma\eta\pi r L \tag{E.2}$$

Where the shear stress shear τ_{shear} is a product of shear rate γ and viscosity η, and the cross section area A_{cross} is half the perimeter πr times the length L.

Alignment Torque The alignment torque T_{shear} can be calculated by integrating the alignment force F_{align} along the length of the tube:

$$T_{shear} = \int F_{align} dL$$

Plug in the expression of F_{align} (Equation E.1) and F_{flow} (Equation E.2):

$$
\begin{aligned}
T_{shear} &= \int F_{align} dL = \int F_{flow} \cos\theta dL \\
&= \int_0^L (\gamma\eta\pi r L)\cos\theta dL = \int_0^L (\gamma\eta\pi r \cos\theta) L dL \\
&= \gamma\eta\pi r \cos\theta \frac{L^2}{2}\Big|_0^L = \gamma\eta\pi r \cos\theta \frac{L^2}{2}
\end{aligned}
\tag{E.3}
$$

Shear Energy The shear energy E_{shear} is calculated by integrating the torque over the angular displacement, θ_i to θ_j:

$$
\begin{aligned}
E_{shear} &= \int T_{shear} d\theta = \int_{\theta_i}^{\theta_j} T_{shear} d\theta \\
&= \int_{\theta_i}^{\theta_j} \gamma\eta\pi r \frac{L^2}{2} \cos\theta d\theta = (\gamma\eta\pi r \frac{L^2}{2}) \sin\theta \Big|_{\theta_i}^{\theta_j} \\
&= (\gamma\eta\pi r \frac{L^2}{2})[\sin\theta_j - \sin\theta_i]
\end{aligned}
\tag{E.4}
$$

And because $0^o \leq \theta_j < \theta_i \leq 90^o$ and thus $\sin\theta_j - \sin\theta_i > 0$, the shear energy is always positive.

Driving Force for Alignment Finally, the driving force for alignment - the ratio of the shear energy over thermal randomization E_{shear}/k_BT, can be derived by plugging in Equation E.4:

$$
\frac{E_{shear}}{k_BT} = \frac{\gamma\eta\pi r \frac{L^2}{2})[\sin\theta_j - \sin\theta_i]}{k_BT} = (\frac{\pi r \frac{L^2}{2}}{k_B}[\sin\theta_j - \sin\theta_i])\frac{\gamma\eta}{T}
$$

Therefore,

$$
\frac{E_{shear}}{k_BT} \propto \frac{\gamma\eta}{T} \tag{E.5}
$$

Which comes to the same conclusion of the Péclet number, that the degree of alignment is proportional to shear rate γ and viscosity η, and inversely to temperature T.

BIBLIOGRAPHY

BIBLIOGRAPHY

[1] S. Iijima. Helical microtubules of graphitic carbon. *Nature*, 354(6348):56–58, 1991. ISSN 0028-0836. doi: Doi10.1038/354056a0.

[2] D. Qian, E. C. Dickey, R. Andrews, and T. Rantell. Load transfer and deformation mechanisms in carbon nanotube-polystyrene composites. *Applied Physics Letters*, 76(20):2868–2870, 2000. ISSN 0003-6951. doi: Doi10.1063/1.126500.

[3] F. H. Gojny, M. H. G. Wichmann, U. Kopke, B. Fiedler, and K. Schulte. Carbon nanotube-reinforced epoxy-compo sites: enhanced stiffness and fracture toughness at low nanotube content. *Composites Science and Technology*, 64(15):2363–2371, 2004. ISSN 0266-3538. doi: DOI10.1016/j.compscitech.2004.04.002.

[4] P. R. Bandaru. Electrical properties and applications of carbon nanotube structures. *Journal of Nanoscience and Nanotechnology*, 7(4-5):1239–1267, 2007. ISSN 1533-4880. doi: Doi10.1166/Jnn.2007.307.

[5] J. W. Che, T. Cagin, and W. A. Goddard. Thermal conductivity of carbon nanotubes. *Nanotechnology*, 11(2):65–69, 2000. ISSN 0957-4484. doi: Doi10.1088/0957-4484/11/2/305.

[6] T. W. Chou, L. M. Gao, E. T. Thostenson, Z. G. Zhang, and J. H. Byun. An assessment of the science and technology of carbon nanotube-based fibers and composites. *Composites Science and Technology*, 70(1):1–19, 2010. ISSN 0266-3538. doi: DOI10.1016/j.compscitech.2009.10.004.

[7] C. A. Martin, J. K. W. Sandler, A. H. Windle, M. K. Schwarz, W. Bauhofer, K. Schulte, and M. S. P. Shaffer. Electric field-induced aligned multi-wall carbon nanotube networks in epoxy composites. *Polymer*, 46(3):877–886, 2005. ISSN 0032-3861. doi: DOI10.1016/j.polymer.2004.11.081.

[8] M. J. Biercuk, M. C. Llaguno, M. Radosavljevic, J. K. Hyun, A. T. Johnson, and J. E. Fischer. Carbon nanotube composites for thermal management. *Applied Physics Letters*, 80(15):2767–2769, 2002. ISSN 0003-6951. doi: Doi10.1063/1.1469696.

[9] M. F. L. De Volder, S. H. Tawfick, R. H. Baughman, and A. J. Hart. Carbon nanotubes: Present and future commercial applications. *Science*, 339(6119):535–539, 2013. ISSN 0036-8075. doi: DOI10.1126/science.1222453.

[10] Q. Zhang, J. Q. Huang, W. Z. Qian, Y. Y. Zhang, and F. Wei. The road for nanomaterials industry: A review of carbon nanotube production, post-treatment, and bulk applications for composites and energy storage. *Small*, 9(8):1237–1265, 2013. ISSN 1613-6810. doi: DOI10.1002/smll.201203252.

[11] Z. Spitalsky, D. Tasis, K. Papagelis, and C. Galiotis. Carbon nanotube-polymer composites: Chemistry, processing, mechanical and electrical properties. *Progress in Polymer Science*, 35(3):357–401, 2010. ISSN 0079-6700. doi: DOI10.1016/j.progpolymsci.2009.09.003.

[12] Y. C. Lan, Y. Wang, and Z. F. Ren. Physics and applications of aligned carbon nanotubes. *Advances in Physics*, 60(4):553–678, 2011. ISSN 0001-8732. doi: Doi10.1080/00018732.2011.599963.

[13] F. M. Blighe, K. Young, J. J. Vilatela, A. H. Windle, I. A. Kinloch, L. B. Deng, R. J. Young, and J. N. Coleman. The effect of nanotube content and orientation on the mechanical properties of polymer-nanotube composite fibers: Separating intrinsic reinforcement from orientational effects. *Advanced Functional Materials*, 21(2):364–371, 2011. ISSN 1616-301X. doi: DOI10.1002/adfm.201000940.

[14] S. U. Khan, J. R. Pothnis, and J. K. Kim. Effects of carbon nanotube alignment on electrical and mechanical properties of epoxy nanocomposites. *Composites Part a-Applied Science and Manufacturing*, 49:26–34, 2013. ISSN 1359-835X. doi: DOI10.1016/j.compositesa.2013.01.015.

[15] J. Y. Ji, G. Sui, Y. H. Yu, Y. X. Liu, Y. H. Lin, Z. J. Du, S. Ryu, and X. P. Yang. Significant improvement of mechanical properties observed in highly aligned carbon-nanotube-reinforced nanofibers. *Journal of Physical Chemistry C*, 113 (12):4779–4785, 2009. ISSN 1932-7447. doi: Doi10.1021/Jp8077198.

[16] Jin Gyu Park, Jesse Smithyman, Chih-Yen Lin, Adam Cooke, Ade W. Kismarahardja, Shu Li, Richard Liang, James S. Brooks, Chuck Zhang, and Ben Wang. Effects of surfactants and alignment on the physical properties of single-walled carbon nanotube buckypaper. *Journal of Applied Physics*, 106(10): 104310, 2009. doi: doi:http://dx.doi.org/10.1063/1.3255901.

[17] P. M. Ajayan, O. Stephan, C. Colliex, and D. Trauth. Aligned carbon nanotube arrays formed by cutting a polymer resin-nanotube composite. *Science*, 265 (5176):1212–1214, 1994. ISSN 0036-8075. doi: DOI10.1126/science.265.5176.1212.

[18] Y. F. Zhu, C. Ma, W. Zhang, R. P. Zhang, N. Koratkar, and J. Liang. Alignment of multiwalled carbon nanotubes in bulk epoxy composites via electric field. *Journal of Applied Physics*, 105(5), 2009. ISSN 0021-8979. doi: Artn054319Doi10.1063/1.3080243.

[19] R. P. Zhang, Y. F. Zhu, C. Ma, and J. Liang. Alignment of carbon nanotubes in poly(methyl methacrylate) composites induced by electric field. *Journal of*

Nanoscience and Nanotechnology, 9(5):2887–2893, 2009. ISSN 1533-4880. doi: Doi10.1166/Jnn.2009.014.

[20] C. Park, J. Wilkinson, S. Banda, Z. Ounaies, K. E. Wise, G. Sauti, P. T. Lillehei, and J. S. Harrison. Aligned single-wall carbon nanotube polymer composites using an electric field. *Journal of Polymer Science Part B-Polymer Physics*, 44 (12):1751–1762, 2006. ISSN 0887-6266. doi: Doi10.1002/Polb.20823.

[21] W. A. Chapkin, D. Q. McNerny, M. F. Aldridge, Y. P. He, W. M. Wang, J. Kieffer, and A. I. Taub. Real-time assessment of carbon nanotube alignment in a polymer matrix under an applied electric field via polarized raman spectroscopy. *Polymer Testing*, 56:29–35, 2016. ISSN 0142-9418. doi: 10.1016/j.polymertesting.2016.09.018.

[22] J. Shaver, A. N. G. Parra-Vasquez, S. Hansel, O. Portugall, C. H. Mielke, M. von Ortenberg, R. H. Hauge, M. Pasquali, and J. Kono. Alignment dynamics of single-walled carbon nanotubes in pulsed ultrahigh magnetic fields. *Acs Nano*, 3 (1):131–138, 2009. ISSN 1936-0851. doi: Doi10.1021/Nn800519n.

[23] D. A. Walters, M. J. Casavant, X. C. Qin, C. B. Huffman, P. J. Boul, L. M. Ericson, E. H. Haroz, M. J. O'Connell, K. Smith, D. T. Colbert, and R. E. Smalley. In-plane-aligned membranes of carbon nanotubes. *Chemical Physics Letters*, 338(1):14–20, 2001. ISSN 0009-2614. doi: Doi10.1016/S0009-2614(01)00072-0.

[24] T. Kimura, H. Ago, M. Tobita, S. Ohshima, M. Kyotani, and M. Yumura. Polymer composites of carbon nanotubes aligned by a magnetic field. *Advanced Materials*, 14(19):1380–1383, 2002. ISSN 0935-9648. doi: Doi10.1002/1521-4095(20021002)14:19⟨1380::Aid-Adma1380⟩3.0.Co;2-V.

[25] M. A. Correa-Duarte, M. Grzelczak, V. Salgueirino-Maceira, M. Giersig, L. M. Liz-Marzan, M. Farle, K. Sierazdki, and R. Diaz. Alignment of carbon nanotubes under low magnetic fields through attachment of magnetic nanoparticles. *Journal of Physical Chemistry B*, 109(41):19060–19063, 2005. ISSN 1520-6106. doi: Doi10.1021/Jp0544890.

[26] G. Korneva, H. H. Ye, Y. Gogotsi, D. Halverson, G. Friedman, J. C. Bradley, and K. G. Kornev. Carbon nanotubes loaded with magnetic particles. *Nano Letters*, 5(5):879–884, 2005. ISSN 1530-6984. doi: Doi10.1021/Nl0502928.

[27] J. E. Fischer, W. Zhou, J. Vavro, M. C. Llaguno, C. Guthy, R. Haggenmueller, M. J. Casavant, D. E. Walters, and R. E. Smalley. Magnetically aligned single wall carbon nanotube films: Preferred orientation and anisotropic transport properties. *Journal of Applied Physics*, 93(4):2157–2163, 2003. ISSN 0021-8979. doi: Doi10.1063/1.1536733.

[28] S. H. Yao, J. K. Yuan, T. Zhou, Z. M. Dang, and J. B. Bai. Stretch-modulated carbon nanotube alignment in ferroelectric polymer

composites: Characterization of the orientation state and its influence on the dielectric properties. *Journal of Physical Chemistry C*, 115(40):20011–20017, 2011. ISSN 1932-7447. doi: Doi10.1021/Jp205444x.

[29] L. Jin, C. Bower, and O. Zhou. Alignment of carbon nanotubes in a polymer matrix by mechanical stretching. *Applied Physics Letters*, 73(9):1197–1199, 1998. ISSN 0003-6951. doi: Doi10.1063/1.122125.

[30] A. Y. Feldman, B. Larin, N. Berestetsky, G. Marom, and A. Weinberg. Microbeam waxd study of orientated crystalline arrays in carbon fiber/cnt-nylon 66 extruded/drawn composites. *Journal of Macromolecular Science Part B-Physics*, 46(1):111–117, 2007. ISSN 0022-2348. doi: Doi10.1080/00222340601044243.

[31] Rebekah Downes, Shaokai Wang, David Haldane, Andrew Moench, and Richard Liang. Strain-induced alignment mechanisms of carbon nanotube networks. *Advanced Engineering Materials*, 2014. ISSN 1527-2648. doi: http://dx.doi.org/10.1002/adem.201400045.

[32] E. Camponeschi, B. Florkowski, R. Vance, G. Garrett, H. Garmestani, and R. Tannenbaum. Uniform directional alignment of single-walled carbon nanotubes in. viscous polymer flow. *Langmuir*, 22(4):1858–1862, 2006. ISSN 0743-7463. doi: Doi10.1021/La052714z.

[33] D. Vennerberg and M. R. Kessler. Anisotropic buckypaper through shear-induced mechanical alignment of carbon nanotubes in water. *Carbon*, 80:433–439, 2014. ISSN 0008-6223. doi: DOI10.1016/j.carbon.2014.08.082.

[34] Y. He and A. I. Taub. Kinetics of carbon nanotube alignment under shear force via real-time polarized raman spectroscopy. *TechConnect Briefs*, 1:69–71, 05 2017.

[35] Y. He and A. I. Taub. Temperature influence on the shear-induced alignment of carbon nanotubes in a polymer composite via real-time polarized raman spectroscopy. *Proceedings of the American Society for Composites (32nd)*, 11 2017. doi: 10.12783/asc2017/15346.

[36] Z. F. Ren, Z. P. Huang, J. W. Xu, J. H. Wang, P. Bush, M. P. Siegal, and P. N. Provencio. Synthesis of large arrays of well-aligned carbon nanotubes on glass. *Science*, 282(5391):1105–1107, 1998. ISSN 0036-8075. doi: DOI10.1126/science.282.5391.1105.

[37] N. Romyen, S. Thongyai, and P. Praserthdam. Alignment of carbon nanotubes in polyimide under electric and magnetic fields. *Journal of Applied Polymer Science*, 123(6):3470–3475, 2012. ISSN 0021-8995. doi: Doi10.1002/App.34692.

[38] Y. Tian, J. G. Park, Q. F. Cheng, Z. Y. Liang, C. Zhang, and B. Wang. The fabrication of single-walled carbon nanotube/polyelectrolyte multilayer

composites by layer-by-layer assembly and magnetic field assisted alignment. *Nanotechnology*, 20(33), 2009. ISSN 0957-4484. doi: Artn335601Doi10.1088/0957-4484/20/33/335601.

[39] X. L. Xie, Y. W. Mai, and X. P. Zhou. Dispersion and alignment of carbon nanotubes in polymer matrix: A review. *Materials Science & Engineering R-Reports*, 49(4):89–112, 2005. ISSN 0927-796X. doi: DOI10.1016/j.mser.2005.04.002.

[40] J. F. Colomer, L. Henrard, P. Lambin, and G. Van Tendeloo. Electron diffraction and microscopy of single-wall carbon nanotube bundles produced by different methods. *European Physical Journal B*, 27(1):111–118, 2002. ISSN 1434-6028. doi: 10.1140/epjb/e20020135.

[41] R. Sharma and Z. Iqbal. In situ observations of carbon nanotube formation using environmental transmission electron microscopy. *Applied Physics Letters*, 84(6):990–992, 2004. ISSN 0003-6951. doi: 10.1063/1.1646465.

[42] A. L. Koh, E. Gidcumb, O. Zhou, and R. Sinclair. Observations of carbon nanotube oxidation in an aberration-corrected environmental transmission electron microscope. *Acs Nano*, 7(3):2566–2572, 2013. ISSN 1936-0851. doi: 10.1021/nn305949h.

[43] Thomas Dieing, Olaf Hollricher, and Jan K. Toporski. *Confocal Raman Microscopy*. Springer, 2011.

[44] R. Saito, A. Gruneis, G. G. Samsonidze, V. W. Brar, G. Dresselhaus, M. S. Dresselhaus, A. Jorio, L. G. Cancado, C. Fantini, M. A. Pimenta, and A. G. Souza. Double resonance raman spectroscopy of single-wall carbon nanotubes. *New Journal of Physics*, 5, 2003. ISSN 1367-2630. doi: Artn157PiiS1367-2630(03)66520-1Doi10.1088/1367-2630/5/1/157.

[45] A. Jorio, M. A. Pimenta, A. G. Souza, R. Saito, G. Dresselhaus, and M. S. Dresselhaus. Characterizing carbon nanotube samples with resonance raman scattering. *New Journal of Physics*, 5, 2003. ISSN 1367-2630. doi: Artn139PiiS1367-2630(03)66293-2Doi10.1088/1367-2630/5/1/139.

[46] B. Lei, K. Ryu, L. G. De-Arco, S. Han, A. Badmaev, D. Farmer, K. Kim, R. Gordon, K. L. Wang, and C. W. Zhou. Raman characterization and polarity tuning of aligned single-walled carbon nanotubes on quartz. *Japanese Journal of Applied Physics*, 49(2), 2010. ISSN 0021-4922. doi: Artn02bc02Doi10.1143/Jjap.49.02bc02.

[47] M. S. Dresselhaus, G. Dresselhaus, R. Saito, and A. Jorio. Raman spectroscopy of carbon nanotubes. *Physics Reports-Review Section of Physics Letters*, 409(2):47–99, 2005. ISSN 0370-1573. doi: DOI10.1016/j.physrep.2004.10.006.

[48] N. Grossiord, J. Loos, J. Meuldijk, O. Regev, H. E. Miltner, B. Van Mele, and C. E. Koning. Conductive carbon-nanotube/polymer composites: Spectroscopic monitoring of the exfoliation process in water. *Composites Science and Technology*, 67(5):778–782, 2007. ISSN 0266-3538. doi: DOI10.1016/j.compscitech.2006.01.035.

[49] Wesley Chapkin. *Electrostatically Induced Carbon Nanotube Alignment for Polymer Composite Applications*. Thesis, University of Michigan, 2017. URL `https://deepblue.lib.umich.edu/handle/2027.42/136945`.

[50] W. Yang, Y. Wang, J. Li, and X. R. Yang. Polymer wrapping technique: an effective route to prepare pt nanoflower/carbon nanotube hybrids and application in oxygen reduction. *Energy & Environmental Science*, 3(1):144–149, 2010. ISSN 1754-5692. doi: Doi10.1039/B916423e.

[51] D. Kim, Y. Kim, K. Choi, J. C. Grunlan, and C. H. Yu. Improved thermoelectric behavior of nanotube-filled polymer composites with poly(3,4-ethylenedioxythiophene) poly(styrenesulfonate). *Acs Nano*, 4(1): 513–523, 2010. ISSN 1936-0851. doi: Doi10.1021/Nn9013577.

[52] I. T. Kim, A. Tannenbaum, and R. Tannenbaum. Anisotropic conductivity of magnetic carbon nanotubes embedded in epoxy matrices. *Carbon*, 49(1):54–61, 2011. ISSN 0008-6223. doi: DOI10.1016/j.carbon.2010.08.041.

[53] K. Lipert, M. Ritschel, A. Leonhardt, Y. Krupskaya, B. Buchner, and R. Klingeler. Magnetic properties of carbon nanotubes with and without catalyst. *International Conference on Magnetism (Icm 2009)*, 200, 2010. ISSN 1742-6588. doi: Artn072061Doi10.1088/1742-6596/200/7/072061.

[54] T. Kimura. Study on the effect of magnetic fields on polymeric materials and its application. *Polymer Journal*, 35(11):823–843, 2003. ISSN 0032-3896. doi: DOI10.1295/polymj.35.823.

[55] E. S. Choi, J. S. Brooks, D. L. Eaton, M. S. Al-Haik, M. Y. Hussaini, H. Garmestani, D. Li, and K. Dahmen. Enhancement of thermal and electrical properties of carbon nanotube polymer composites by magnetic field processing. *Journal of Applied Physics*, 94(9):6034–6039, 2003. ISSN 0021-8979. doi: 10.1063/1.1616638.

[56] C. G. Ma, H. Y. Liu, X. S. Du, L. T. Mach, F. Xu, and Y. W. Mai. Fracture resistance, thermal and electrical properties of epoxy composites containing aligned carbon nanotubes by low magnetic field. *Composites Science and Technology*, 114:126–135, 2015. ISSN 0266-3538. doi: 10.1016/j.compscitech.2015.04.007.

[57] Ronald G. Larson. *The structure and rheology of complex fluids*. Topics in chemical engineering. Oxford University Press, New York, 1999.

ISBN 019512197X (cloth alk. paper). URL http://www.loc.gov/catdir/enhancements/fy0603/98019940-d.html.

[58] J. P. Casey, S. M. Bachilo, C. H. Moran, and R. B. Weisman. Chirality-resolved length analysis of single-walled carbon nanotube samples through shear-aligned photoluminescence anisotropy. *Acs Nano*, 2(8):1738–1746, 2008. ISSN 1936-0851. doi: 10.1021/nn800351n.

[59] R. Allen, G. G. Fuller, and Z. N. Bao. Aligned swnt films from low-yield stress gels and their transparent electrode performance. *Acs Applied Materials & Interfaces*, 5(15):7244–7252, 2013. ISSN 1944-8244. doi: 10.1021/am401592v.

[60] A. W. K. Ma, M. R. Mackley, and S. S. Rahatekar. Experimental observation on the flow-induced assembly of carbon nanotube suspensions to form helical bands. *Rheologica Acta*, 46(7):979–987, 2007. ISSN 0035-4511. doi: 10.1007/s00397-007-0183-x.

[61] R. Allen, Z. A. Bao, and G. G. Fuller. Oriented, polymer-stabilized carbon nanotube films: influence of dispersion rheology. *Nanotechnology*, 24(1), 2013. ISSN 0957-4484. doi: Artn01570910.1088/0957-4484/24/1/015709.

[62] R. Perez, S. Banda, and Z. Ounaies. Determination of the orientation distribution function in aligned single wall nanotube polymer nanocomposites by polarized raman spectroscopy. *Journal of Applied Physics*, 103(7), 2008. ISSN 0021-8979. doi: Artn07430210.1063/1.2885347.

[63] J. A. Fagan, J. R. Simpson, B. J. Landi, L. J. Richter, I. Mandelbaum, V. Bajpai, D. L. Ho, R. Raffaelle, A. R. H. Walker, B. J. Bauer, and E. K. Hobbie. Dielectric response of aligned semiconducting single-wall nanotubes. *Physical Review Letters*, 98(14), 2007. ISSN 0031-9007. doi: ARTN14740210.1103/PhysRevLett.98.147402.

[64] R. Haggenmueller, H. H. Gommans, A. G. Rinzler, J. E. Fischer, and K. I. Winey. Aligned single-wall carbon nanotubes in composites by melt processing methods. *Chemical Physics Letters*, 330(3-4):219–225, 2000. ISSN 0009-2614. doi: Doi10.1016/S0009-2614(00)01013-7.

[65] 2013. URL http://www.compositesworld.com/articles/market-outlook-surplus-in-carbon-fibers-future.

[66] Matthew Chong. Icis pricing epoxy resins (asia). Report, ICIS, 2014.

[67] J. B. Bai and A. Allaoui. Effect of the length and the aggregate size of mwnts on the improvement efficiency of the mechanical and electrical properties of nanocomposites - experimental investigation. *Composites Part a-Applied Science and Manufacturing*, 34(8):689–694, 2003. ISSN 1359-835X. doi: Doi10.1016/S1359-835x(03)00140-4.

[68] D. C. Davis, J. W. Wilkerson, J. A. Zhu, and D. O. O. Ayewah. Improvements in mechanical properties of a carbon fiber epoxy composite using nanotube science and technology. *Composite Structures*, 92(11):2653–2662, 2010. ISSN 0263-8223. doi: DOI10.1016/j.compstruct.2010.03.019. URL <GotoISI>://WOS:000279301300005.

[69] Hexcel. Hexply prepreg technology. Report, Hexcel, January 2013 2013. URL http://www.hexcel.com/Resources/DataSheets/Brochure-Data-Sheets/Prepreg_Technology.pdf.

[70] S. Zaric, G. N. Ostojic, J. Kono, J. Shaver, V. C. Moore, R. H. Hauge, R. E. Smalley, and W. Xing. Estimation of magnetic susceptibility anisotropy of carbon nanotubes using magnetophotoluminescence. *Nano Letters*, 4(11):2219–2221, 2004. ISSN 1530-6984. doi: Doi10.1021/Nl0486012.